

Paleoceanography and Paleoclimatology

RESEARCH ARTICLE

10.1029/2020PA003981

Key Points:

- Sedimentary archives from the Sabrina Coast continental slope document high-amplitude glacial cycles since the mid-Pleistocene transition
- Sedimentation and primary productivity are primarily controlled by sea ice extent and ice sheet position on the continental shelf
- These controls are amplified since the MPT and as a consequence influence sedimentation around the entire Antarctic Margin concurrently

Supporting Information:

- Supporting Information S1

Correspondence to:

L. Holder,
l.holder18@imperial.ac.uk

Citation:

Holder, L., Duffy, M., Opdyke, B., Leventer, A., Post, A., O'Brien, P., & Armand, L. K. (2020). Controls since the mid-Pleistocene transition on sedimentation and primary productivity downslope of Totten Glacier, East Antarctica. *Paleoceanography and Paleoclimatology*, 35, e2020PA003981. <https://doi.org/10.1029/2020PA003981>

Received 14 MAY 2020

Accepted 2 DEC 2020

Accepted article online 9 DEC 2020

Controls Since the mid-Pleistocene Transition on Sedimentation and Primary Productivity Downslope of Totten Glacier, East Antarctica

L. Holder^{1,2} , M. Duffy³ , B. Opdyke² , A. Leventer³ , A. Post⁴ , P. O'Brien⁵ , and L. K. Armand² 

¹Department of Earth Science and Engineering, Imperial College London, Kensington, London, UK, ²Research School of Earth Sciences, Australian National University, Canberra, ACT, Australia, ³Department of Geology, Colgate University, Hamilton, NY, USA, ⁴Geoscience Australia, Canberra, ACT, Australia, ⁵Department of Earth and Planetary Sciences, Macquarie University, North Ryde, New South Wales, Australia

Abstract The rapidly thinning Totten Glacier on the Sabrina Coast, East Antarctica, is the primary drainage outlet for ice within the Aurora Subglacial Basin, which could destabilize under the current atmospheric warming trend. There is growing need for direct geological evidence from the Sabrina Coast to frame late twentieth century Totten melting in the context of past warm climate analogs. Addressing this need, sediment archives were recovered from two sites on the Sabrina Coast slope and rise that record changes in terrigenous sedimentation and primary productivity in the region over glacial cycles since the mid-Pleistocene transition (MPT). This research presents physical properties, grain size, diatom abundance and assemblages, and geochemical analysis from the two sites to determine how the processes that control sedimentation change between glacial and interglacial phases. The stratigraphic sequences in both cores record cyclic variations in physical properties and diatom abundances, which radiocarbon and biostratigraphic chronologies reveal as 100 Kyr glacial-interglacial cyclicity. During glacials, terrigenous sediment deposition is enhanced by advanced grounded ice on the shelf, while primary productivity is restricted due to permanent summer sea ice extending past the continental slope. During interglacials, pelagic sedimentation suggests high surface productivity associated with contractions of regional sea ice cover. Comparison with post-MPT slope records from Wilkes Land and the Amundsen Sea shows that this pattern is consistent in slope sediments around the margin. The higher-amplitude variations in Antarctic ice volume and sea ice extent post-MPT ensure that these signals are pervasive around the Antarctic margin.

Plain Language Summary To improve predictions of future Antarctic ice sheet behavior, knowledge of how Antarctica responded in the past, particularly when temperatures were similar to or higher than today, is required. Geological records recovered from ice proximal sediments can provide this information. The sediments record variations in physical, chemical, and biological properties and therefore act as indicators of paleoenvironmental change. Two sediment cores recovered from the Sabrina Coast continental slope and rise, East Antarctica, are used to study past changes in sediment deposition, as influenced by glacial and oceanographic processes. The two archives show clear variations in sediment composition and microfossil assemblage between glacial and interglacial conditions on 100 Kyr timescales over the last 350,000 years, driven by the movement of the ice sheet across the continental shelf and the extent of sea ice cover. This research suggests that the drivers of sedimentation and the patterns revealed in slope sediments are consistent around the Antarctic margin due to the larger variations in climate since the mid-Pleistocene transition.

1. Introduction

Following the mid-Pleistocene transition (~700 Kyr; MPT), Earth's climate shifted to a lower frequency (~100 Kyr) and higher-amplitude pacing of glacial cycles (Clark et al., 2006; McClymont et al., 2013). This gave rise to the “super interglacials” including Marine Isotopic Stages (MIS) 5e and 9 (124–119 and 337–300 Kyr, respectively), which are of particular interest because they provide recent context for past

warm periods when sea levels were significantly higher than today (Dutton et al., 2015; Lüthi et al., 2008; Raymo & Mitrovica, 2012). Furthermore, the higher-amplitude swings in the global benthic $\delta^{18}\text{O}$ record between interglacial maxima and glacial minima post-MPT indicate that continental ice volume expanded and contracted to the greatest extent since the Miocene (Lisiecki & Raymo, 2005; Raymo et al., 2006). It was originally thought that the East Antarctic Ice Sheet (EAIS) did not significantly contribute to post-MPT sea level highstands (Dutton et al., 2015; Kopp et al., 2009; Raymo & Mitrovica, 2012). However, observations (e.g., Anderson et al., 2014; Weber et al., 2014; Wilson et al., 2018) and recent modeling suggest a varied and dynamic response of the EAIS during post-MPT interglacials, where significant thinning and retreat may have occurred in basins with marine-terminating ice sheets (DeConto & Pollard, 2016; Golledge et al., 2012; Pollard et al., 2015). For example, seaward of the Wilkes Subglacial Basin, IODP Site 1361 documented changes in sediment provenance to more inland terrains during peak interglacial warmth of the late Pleistocene (Wilson et al., 2018). Despite this, the behavior of the EAIS is not uniform in response to interglacial warmth. In the Prydz Channel Trough Mouth Fan at ODP site 1167, lithostratigraphy, grain size, and $\delta^{18}\text{O}$ stratigraphy have documented repeated large-scale advance and retreat of the Lambert Glacier-Amery ice shelf prior to the MPT but showed that no advance to the shelf break occurred post-MPT (Passchier et al., 2003; Theissen et al., 2003). Hence, expanding upon the current spatial coverage of direct geological evidence from climatically vulnerable regions of the East Antarctic margin is important to improve our understanding of ice sheet response (Domack et al., 1998; Escutia et al., 2011; Hillenbrand et al., 2009; Lucchi et al., 2002; Passchier et al., 2003).

One region of interest is the Sabrina Coast, where 21st century melting of the Totten Glacier is the highest on the East Antarctic margin (Flament & Rémy, 2012; Li et al., 2015; Rignot et al., 2019). The Totten Glacier constitutes the primary drainage outlet for the Aurora Subglacial Basin (ASB), which holds 287,000 km³ of ice (Roberts et al., 2011; Wright et al., 2012; Young et al., 2011) that equates to 3.5 m of sea level equivalent ice (Greenbaum et al., 2015). The presence of relatively warm modified Circumpolar Deep Water (mCDW) entering into the ice shelf cavity via a glacially carved cross shelf trough has the potential to drive both basal ice shelf melt and melting at the deep grounding line (Fernandez et al., 2018; Greenbaum et al., 2015; Gulick et al., 2017; Nitsche et al., 2017; Rintoul et al., 2016). The observed vulnerability of this region of the EAIS to 21st century warming requires proximal geological evidence to examine ocean-ice sheet interactions during past warm periods to contextualize the modern scenario and predict the response of Totten Glacier to future climate change. Recently, sedimentary archives were recovered from the Sabrina Coast shelf dating back to the Paleocene which, together with geophysical data, revealed dynamic behavior of the EAIS in the ASB catchment (Gulick et al., 2017). However, no such sedimentary records exist from the continental slope environment seaward of the Sabrina Coast, where seismic data indicate that sediment from the ASB has accumulated for ~34 million years (Close et al., 2007; Donda et al., 2007).

To address the lack of records from the Sabrina Coast slope region of East Antarctica, sedimentary records were recovered during the Australian-led IN2017-V01 research expedition. This paper presents the findings from two sites, which document multiple glacial-interglacial cycles from the middle Pleistocene to Holocene. Lithostratigraphy, physical properties, and diatom assemblage records were generated from paired multi-, Kasten, and piston cores at Sites A005 and C012 at depths of 2,163 and 3,100 m respectively (Figure 1). These records document changes in paleoproductivity and sedimentation at the Sabrina Coast, as influenced by the interplay of local oceanographic and cryospheric conditions. Lithostratigraphic sequences in Antarctic slope sediments have been well described in multiple regions of the Antarctic Margin including Wilkes Land (Escutia et al., 2011), Prydz Bay (Domack et al., 1998; Passchier et al., 2003), the Antarctic Peninsula (Lucchi et al., 2002; Pudsey, 2000), and the Ross Sea (Ceccaroni et al., 1998; Kim et al., 2020) among others. The described lithostratigraphy shows a common pattern with lighter brown diatom-rich silty clays commonly ascribed to interglacial periods and darker gray diatom-poor clays indicating glacial periods (Hillenbrand et al., 2009). These interpretations are supported by concurrent variations in the physical, sedimentological, and geochemical characteristics of the sediments. Magnetic susceptibility (MS) and Natural Gamma Radiation (NGR) have both been used extensively as indicators of terrigenous content within sediments and often co-vary with grain size changes (Ceccaroni et al., 1998; Lee et al., 2017; Hillenbrand et al., 2009). Studies on XRF bulk geochemical data have shown using principal component analysis that Ba and Ca abundance are consistently linked with high biogenic content in sediments while Al, Si, K, Ti, and Fe are related to lithogenic content (Jimenez-Espejo et al., 2020; Wilson et al., 2018).

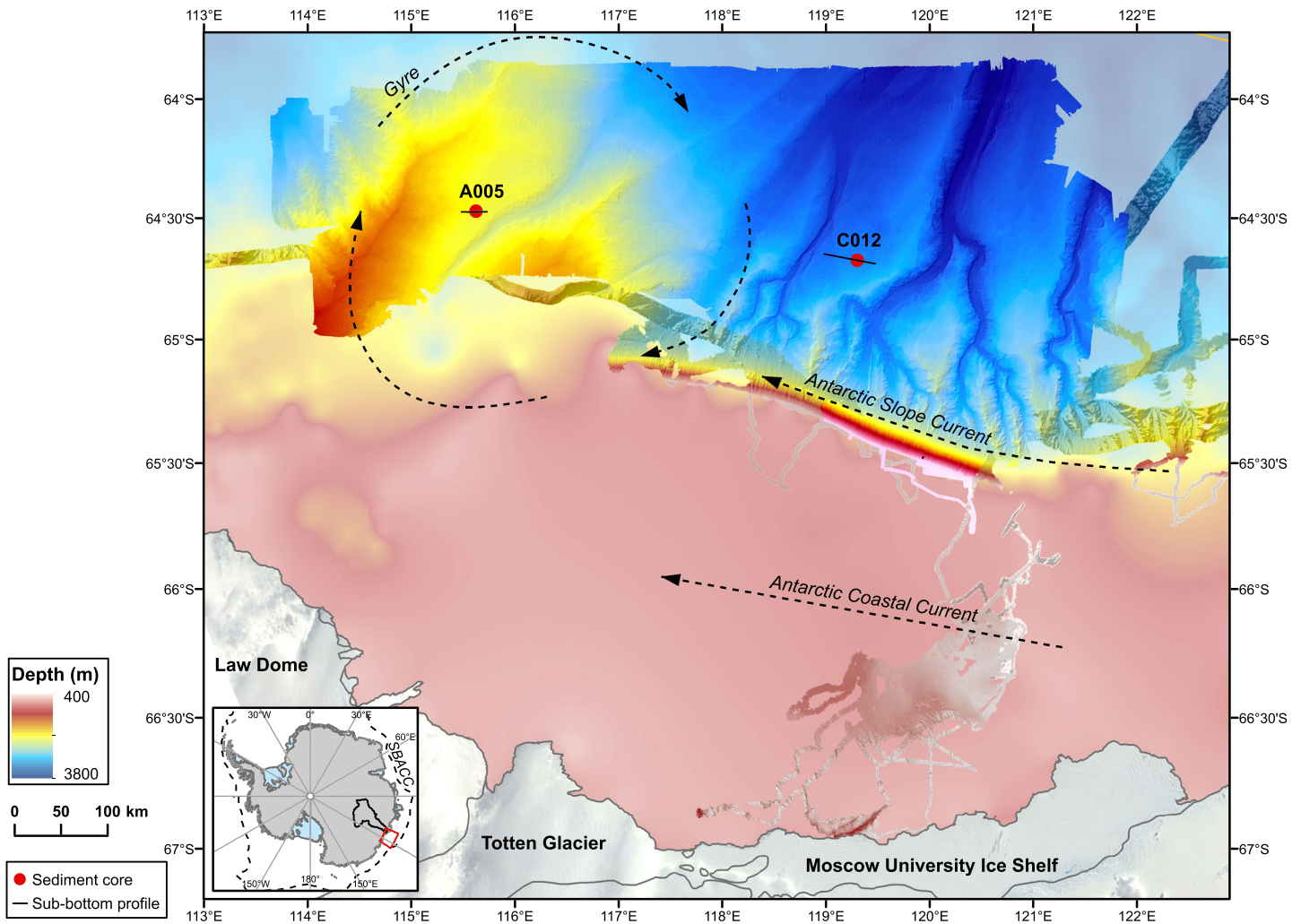


Figure 1. Study region on the Sabrina Coast continental shelf with multibeam bathymetric swath map of the continental shelf, slope, and rise overlying the IBSCO digital bathymetric model (Armand et al., 2018; Arndt et al., 2013; Gulick et al., 2017; Spence et al., 2017). Red dots indicate the two coring locations A005 and C012 which are the focus of this paper. Black lines across the coring locations are the sub-bottom profile lines seen in Figure 2. Major oceanographic features are also visualized including the gyre identified by Wakatsuchi et al. (1994). The Southern Boundary of the ACC is just to the north of the study location but is represented on the Antarctic inset (lower left).

Unlike the North Atlantic, measurements of Ice Rafted Debris (IRD) in Antarctic sediment archives show no pervasive signal of ice rafting but instead vary between regions, perhaps highlighting the non-uniform response of each sector to climatic change (Cowan et al., 2008; Hillenbrand et al., 2009; Wilson et al., 2018). The abundance and assemblage of diatoms within sedimentary sequences are used as indicators of primary productivity, sea ice cover, and reworking of older sediments by glacial and oceanographic processes, in addition to providing valuable biostratigraphic constraints on chronology (Bohaty et al., 1998; Cody et al., 2008; Konfirst et al., 2012; Zielinski & Gersonde, 2002). For example, diatom species such as *Fragilariopsis kerguelensis* and *Thalassiosira lentiginosa* are commonly used as indicators of the Permanently Open Ocean Zone (POOZ) as they occur in maximum abundance between the Polar Front and the summer sea ice edge (Crosta et al., 2005). While the geographical range of the species *Fragilariopsis curta* is confined southward of maximum winter sea ice extent making their presence an indicator of sea ice (Armand et al., 2005; Gersonde & Zielinski, 2000; Leventer, 1998). The aforementioned proxy data are used to reconstruct the post-MPT history of sedimentation and paleoproductivity of the slope environment at the Sabrina Coast region and are placed in context with similar records from different Antarctic slope settings.

For Antarctic sedimentary archives spanning the middle to late Pleistocene, the development of an accurate age model to assess the timing of changes can be challenging. Traditional methods of developing chronology by correlating core depths with absolute age markers such as paleomagnetic reversals, biostratigraphic datums, and the global $\delta^{18}\text{O}$ stratigraphy are limited by the scarcity of datums during the middle to late Pleistocene and the paucity of carbonate in Antarctic sediments. The close correlation between the global benthic $\delta^{18}\text{O}$ LR04 timescale and records of Ba/Al (Presti et al., 2011) and diatom absolute abundance (Konfirst et al., 2012) on the Antarctic margin has also been used to generate secondary tie points. One method of increasing the number of absolute age markers, while limited to the last 55 ka, is through radiocarbon (^{14}C) dating of inorganic carbon in planktonic foraminifera (Domack et al., 2005; Kim et al., 2020; Skinner et al., 2010). In order to use radiocarbon dates as absolute age markers, one must first convert the ^{14}C age of a sample into calendar ages. For marine samples, this requires knowledge of the variable ^{14}C age in the coeval atmosphere and the relative depletion in the local surface ocean ^{14}C reservoir, known as the marine reservoir age (or R value). The R value in the surface ocean mixed layer varies significantly both spatially and temporally, due to differences in air-sea gas exchange and ocean circulation, with the highest modern values ($\sim 1,000$ years) seen in Antarctic waters (Key et al., 2004). The traditional method to account for the variability in R value is by calibrating marine ^{14}C ages against the globally averaged marine calibration curve Marine20 (Heaton et al., 2020). This calibration takes into account the temporal variability in the “globally averaged” (defined as the region between 40°S and $40/50^\circ\text{N}$) R value relative to the ^{14}C age of CO_2 in the Northern Hemispheric atmospheric (IntCal20; Reimer et al., 2020). In order to also account for spatial variability in R values, the calibration requires a constant regional R value (ΔR) correction, being the difference between the coeval local and globally averaged R value. However, the local R value, and hence ΔR , in polar regions is likely to exhibit more extreme temporal variability, by more than 1,000 years during past glacial periods, due to extreme changes in sea ice extent, deep ocean upwelling, and wind speeds (Butzin et al., 2017, 2005; Skinner et al., 2010, 2017, 2019). Therefore, Heaton et al. (2020) suggested that because of the constant ΔR correction implicit in Marine20, its use for calibrating polar radiocarbon dates was unsuitable. While alternative approaches have been suggested to handle the extreme temporal variability in R value in polar regions (Alves et al., 2019; Butzin et al., 2017; Skinner et al., 2010, 2019), the merit in doing so must be weighed against the required resolution of the age model as each approach introduces new uncertainties.

1.1. Oceanographic Setting

The study area is located south of the eastward flowing southern boundary of the Antarctic Circumpolar Current (ACC) (Figure 1; Orsi et al., 1995). South of the Antarctic Polar Front, Ekman divergence from the Southern Ocean westerly wind belt upwells warm ($>0^\circ\text{C}$), saline (34.70–34.75) Circumpolar Deep Water (CDW) to the level of the continental shelf break along the Sabrina Coast (Bindoff et al., 2000; Williams et al., 2011). A cyclonic gyre identified just north of the Sabrina shelf break, centered on 115°E , is thought to be generated by a bathymetric high in this region (Wakatsuchi et al., 1994). Along the upper continental slope between 750 and 1,250 m water depth, the westward flowing Antarctic Slope Current (ASC) forms the boundary between CDW and Antarctic Surface Water (AASW) (Peña-Molino et al., 2016; Williams et al., 2011). Along the lower slope, a westward flowing bottom current comprising Antarctic Bottom Water (AABW) originating from the Adelie Land is also present (Rintoul, 1985). The strength of the ASC controls the exchange of heat across the continental shelf and hence acts as a buffer for the Antarctic ice sheet against warmer ocean waters (Thompson et al., 2018). On the Sabrina Coast, intrusion of modified CDW (mCDW) onto the continental shelf is aided by local bathymetric depressions along the shelf break (Nitsche et al., 2017). Shelf waters of the Sabrina Coast are shown to resemble those of the Amundsen and Bellingshausen Seas, with relatively warm (up to 0.3°C) mCDW shown to be widespread on the continental shelf (Silvano et al., 2017). Hence, the Totten Glacier is considered one of the most vulnerable to modern changes in ocean heat flux due to a deep ice shelf grounding line (Fretwell et al., 2013; Greenbaum et al., 2015), strong wind-driven upwelling of modified CDW (Greene et al., 2017), variable shelf break bathymetry (Nitsche et al., 2017), and low levels of sea ice and Dense Shelf Water production in the Dalton Polynya (Tamura et al., 2008).

During past glacial periods, the increase in Southern Ocean stratification was thought to have been due to an equatorward shift and reduction in the intensity of the Southern Hemisphere westerly wind belt (Anderson

et al., 2009; Toggweiler & Russell, 2008). However, it is still unclear how the westerly winds changed in response to the glacial climate and their influence on Southern Ocean circulation (Kohfeld et al., 2013; Sime et al., 2013). Instead, observations and modeling have shown an expanded glacial sea ice extent limited interhemispheric deep water mixing, essentially separating the deep and shallow overturning cells within the Southern Ocean (Ferrari et al., 2014; Gersonde et al., 2005; Stephens & Keeling, 2000). Enhanced sea ice cover also reduces primary productivity in surface waters by blocking the availability of light, hence reducing biogenic deposition (Arrigo et al., 2008). Current speeds within the core of the ACC are thought to be similar or even stronger than today (Matsumoto et al., 2001). However, south of the glacial sea ice extent ($\sim 56^{\circ}\text{S}$), the strength of the southern boundary of the ACC is suggested to have significantly weakened, a process also modulated by sea ice (McCave et al., 2014). This could also affect the strength of the ASC and the associated along-slope transport at the study location during glacial periods. Conflicting evidence exists for changes in the westward flowing bottom currents associated with AABW originating from the Adelie Land shelf. Jimenez-Espejo et al. (2020) argue that AABW production shuts down during peak glacials, as seen by low oxygen conditions in Antarctic slope sediments, while Basak et al. (2018) use neodymium isotopes to argue for an expansion of AABW from the Ross Sea during the LGM. In the modern context, the Dalton Polynya on the Sabrina coast shelf is not capable of producing AABW because of low sea ice production rates (Tamura et al., 2008; Williams et al., 2011). However, the formation of AABW and its influence on slope sediments during glacial conditions are still unknown in this region of the Antarctic.

2. Materials and Methods

2.1. Regional Setting

Survey IN2017_V01 took place aboard the Australian RV *Investigator*, from January to March 2017; complete details are recorded in the post-cruise report (Armand et al., 2018). In brief, a comprehensive seafloor survey was conducted on the Sabrina Coast continental slope and rise, and bathymetry was recorded by Kongsberg EM122 and EM710 multibeam echosounders and Kongsberg SBP120 sub-bottom profiler in order to target sites for coring operations (Figures 1 and 2). The survey area exhibits a depositional system similar to many parts of the Antarctic margin (Caburlo et al., 2010; Escutia et al., 2000) with a series of dendritic submarine canyons, which form transport pathways for sediment from the shelf to the rise, separated by overbank deposits, east to west transport of suspended sediment by along-slope currents, and a larger sediment depocenter further west (O'Brien et al., 2020; Post et al., 2020). Sedimentation in the region is controlled by multiple factors, including sediment gravity flows, primary productivity, reworking, and entrainment of fine-grained material in along-slope currents and ice rafting of terrigenous debris (Anderson et al., 1984; Escutia et al., 2003; Lucchi et al., 2002; O'Brien et al., 2020; Patterson et al., 2014). The balance of each of these processes is likely to vary significantly between glacial and interglacial phases making these cores good locations to study changes in deposition related to oceanographic and glacial processes through glacial-interglacial cycles.

Sites A005 ($64^{\circ}28.26'\text{S}$, $115^{\circ}37.38'\text{E}$, water depth 2,161 m) and C012 ($64^{\circ}40.517'\text{S}$, $119^{\circ}18.072'\text{E}$, water depth 3,104 m) are located on ridge plateau and ridge flank low-slope geomorphic environments identified by O'Brien et al. (2020). These locations were targeted for coring operations based on sub-bottom profile imagery that revealed a well-stratified sediment package, with strong penetration into the subsurface and no signs of disturbance from slumping or mass movement at the core site. Sub-bottom profiles were loaded as segy files into SeiSee for visualization (Figure 2). At Sites A005 and C012, the cores included in this study are as follows: multi-core A005-MC01 (0.3 m), Kasten core A005-KC02 (2.40 m), piston core A005-PC01 (13.55 m), multi-core C012-MC03 (0.30 m), Kasten core C012-KC04 (2.49 m), and piston core C012-PC05 (16.28 m).

2.2. Physical Properties and Grain Size Analysis

Piston cores were scanned for physical properties including MS and NGR at 5 cm intervals with a GEOTEK Multi-Sensor Core Logger. Kasten core MS was measured at 2 cm intervals on U-channels taken from the core using a Bartington MS Meter MS3 point sensor; data were duplicated by passing the U-channel through a 45 mm loop sensor, both methods using BARTSOFT software (v.1.7.1). Scanning XRF data were obtained on piston cores at 5 cm resolution using the Avaatech core scanner located at the Research School of Earth Sciences at the Australian National University. Core ends, voids, and lonestones were excluded from the

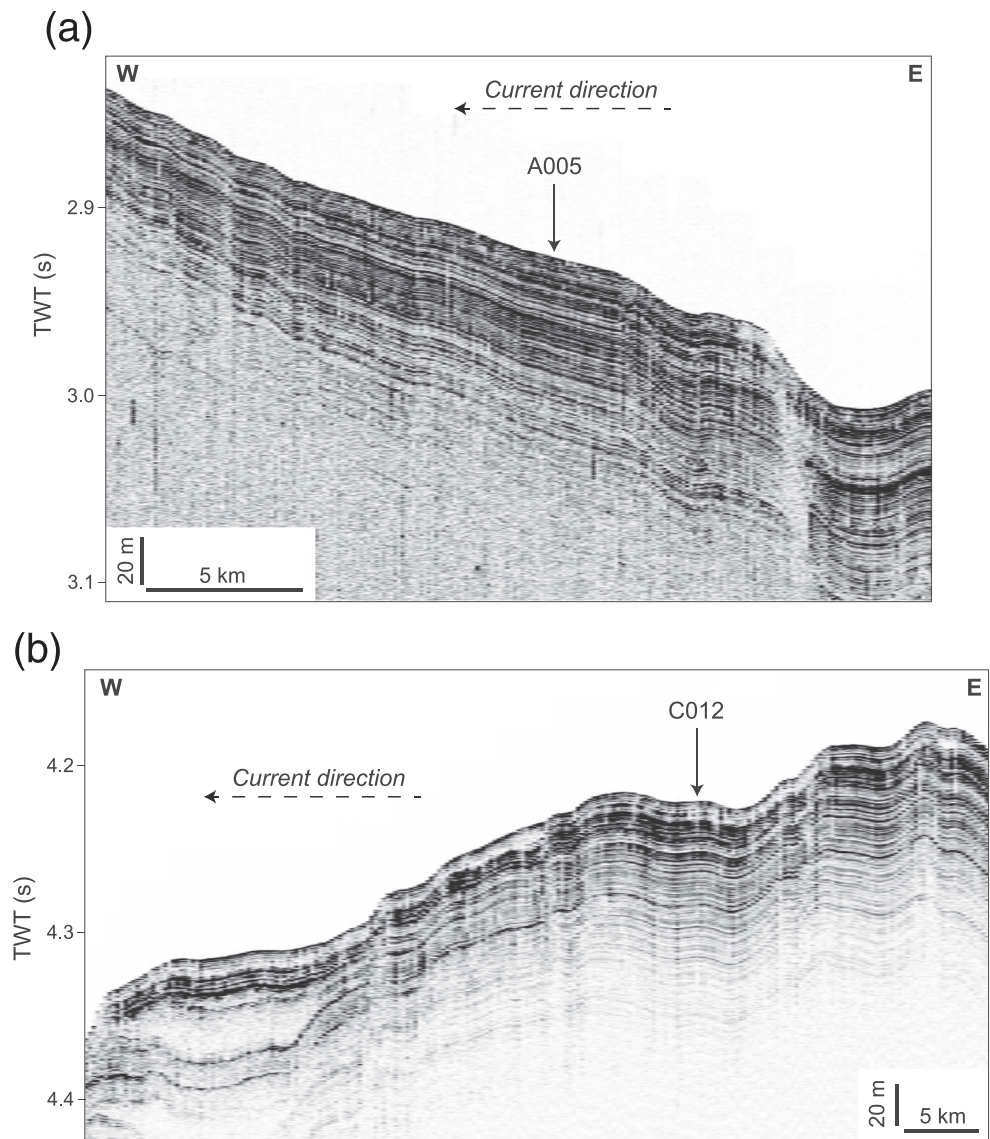


Figure 2. Sub-bottom profiles from the coring locations (a) Site A005 and (b) Site C012. Vertical scale bar calculated using a sediment velocity of $1,600 \text{ m s}^{-1}$ (Stagg et al., 2004). Dashed arrow indicates the direction of bottom flows toward the west.

scan. Ba/Al count ratios were derived from the raw count data. The resulting curves were compared to those produced by taking the natural log of the ratios as recommended by Weltje and Tjallingii (2008). As there was no obvious difference between the downcore variations using the two methods, we present the count ratios in order to allow direct comparison with Wilson et al. (2018).

Sub-samples of 2 g of sediment were taken at 10 cm depth intervals for grain size analysis. Biogenic siliceous opal was not dissolved in the sub-samples prior to grain size analysis. Aliquots of wet sample were pipetted for grain size analysis of the 0–2 mm size fraction using a Malvern Mastersizer 2000 laser particle sizer at Geoscience Australia to calculate the volume weighted percentage of particles in the sample. Samples were subjected to identical treatment in the calibrated Malvern Dispersion Unit to ensure that the silt-clay ratios would not be affected by disaggregation artifacts (Tan et al., 2017). Duplicates were run at 1 m intervals to test for consistency in measured grain size, and each sample was analyzed three times to determine measurement variance ($<0.4\%$ across clay, silt, and sand fractions). Glass bead standards were run every 50–100 analyses for instrument calibration. Results were pooled to determine changes in the silt, clay, sand, and gravel fractions down core.

Table 1
Results From Radiocarbon Dating of *N. pachyderma* (s) Samples

Sample ID core depth (cm)	¹⁴ C age (Kyr BP) ^a	Uncertainty (±Kyr BP) ^a	Calibrated ¹⁴ C age (cal. Kyr BP) ^b	Uncertainty (±2σ cal. Kyr BP) ^b	Reservoir corrected ¹⁴ C age (cal. Kyr BP) ^c	Uncertainty (±2σ cal. Kyr BP) ^c
C012-MC03_ 0-1	1.08	0.028	0.93 ^d	0.03	0.52 ^e	0.11
C012-KC04_ 250-252	34.58	0.39	38.73	0.96	38.09	1.04
C012-PC05_ 245-246	30.98	0.25	34.60	0.51	34.12	0.55
C012-PC05_ 265-266	37.70	0.57	41.39	0.74	41.02	0.89
C012-PC05_ 285-286	46.50	1.69	48.50	3.90	47.87	4.02

^aRaw uncalibrated ¹⁴C ages. ^bCalibrated ¹⁴C ages on the Marine20 calibration curve from Heaton et al. (2020) using the CALIB online calibration tool <http://calib.org/calib/> with no correction for ΔR. ^cCalibrated and corrected ¹⁴C ages using a constant ΔR correction of 519 ± 110 cal. years BP from the C012-MC03 core top. ^dThe calculated local R value from the C012-MC03 core top being the difference between the raw ¹⁴C age and the SHCal20 ¹⁴C age at 0 BP (Hogg et al., 2020). ^eThe calculated ΔR value being the difference between the local R value and the “global average” R value at 0 BP (Heaton et al., 2020). MC = multi-core, KC = Kasten core, PC = piston core.

Sub-samples of 20 cc of sediment at continuous 10 cm intervals throughout C012-PC05 were used to determine the weight % of the coarse sand fraction (300–2 mm) relative to the mass of the bulk dried sediment. These samples were wet sieved and weighed following the method of Patterson et al. (2014). Biogenic silica and carbonate were not removed from the coarse sand fraction because these grains comprise a comparatively small weight component within the 300–2 mm size fraction compared with siliciclastic material and do not bias the overall signal.

In order to assess how much, if any, material had been lost from the top of the Kasten core and piston core during coring operations and reaffirm the continuity of the records, a composite depth section was generated between multi-, Kasten, and piston cores at each location. MS was used to correlate the cores and generate composite depth using the QAnalyseries software (Kotov & Pälke, 2018). Tie points were visually picked so as to align the similar features between the MS records. First, the Kasten core was aligned with the multi-core as a target since the multi-core will preserve the most accurate representation of the core top. Following this, the piston core was aligned on the new composite depth scale of the Kasten core (supporting information Figures S3 and S4). The amount of material lost from the core top of the Kasten and piston cores was assessed by measuring the offset in MS features from the multi-core.

2.3. Diatom Analysis

Sub-samples for diatom analysis were taken at 10 cm intervals in biogenic sections and 20 cm intervals from terrigenous sediments for all cores. Quantitative diatom slides were prepared according to the settling technique of Warnock and Scherer (2014). Cover slips were adhered to the slides using Norland Optical Adhesive #61. Slides were observed under Olympus CX31, BX60, and Zeiss Primo Star light microscopes, using a 100X oil immersion objective for a total magnification of 1,000X. A minimum of 400 valves or 10 transects were counted for each slide, depending on the diatom absolute abundance. Biogenic samples were relatively diatom rich; consequently counts of 400 specimens were possible. However, most terrigenous samples were diatom poor. For these samples, 10 transects were counted, as has been done in previous studies of sediments with very low diatom concentrations (Rebesco et al., 2014). Valves were only counted if >50% complete. Diatoms were identified to species level where possible (Armand et al., 2005; Cefarelli et al., 2010; Crosta et al., 2005). Occurrences of biostratigraphic markers were noted and tallied concurrently. In addition to the transect work conducted at 1,000X magnification, to provide greater confidence in evaluating the last occurrence of *Hemidiscus karstenii*, biostratigraphic marker for the MIS 7/MIS 6 boundary, an additional four transects were examined at lower magnification, 400X, in order to view a greater portion of the slides. Since *H. karstenii* are relatively large and robust, they are clearly identifiable at this magnification. These extra counts (Table 1 and Figure S1) were conducted from 440–790 cm in PC01 and from 400–1,020 cm in PC05, intervals that, based on the MS data, were thought to cover this time interval. In addition, count data for *Rouxia leventerae* are provided in supporting information Figure S2. These data are included as support for the last occurrence of *R. leventerae* at the MIS 5/6 boundary and to illustrate the difficulty in this marker given the increased relative proportion of reworked specimens in sections of the core with extremely low diatom abundance. Finally, species were considered extinct when no longer observed stratigraphically higher than extinction boundaries as identified by Cody et al. (2008).

2.4. Age Model

Radiocarbon dating was completed at the Australian National University on samples of the planktic foraminifera *Neogloboquadrina pachyderma* (s). Between 5 and 10 mg of carbonate material was used (Fallon et al., 2010). In total, five dates were obtained from the three cores at Site C012. The core top of the multi-core C012-MC03 contains the most recently deposited foraminiferal material, and hence, in order to estimate the regional Marine Reservoir Age of the surface ocean (ΔR), it was assumed that the true age of the core top was the year 0 BP. The ΔR value was estimated using the ^{14}C age of SHCal20 (Hogg et al., 2020) and the Global Average Marine Reservoir Age ($R_{\text{globalave}}$) from Marine20 (Heaton et al., 2020) at 0 BP. The foraminiferal material from C012-MC03 was not stained in the picking process, and hence, we cannot rule out contamination from reworked old carbon.

Additional radiocarbon dates were obtained from C012-KC04 and C012-PC05 in the carbonate rich layer 200–300 cm downcore and used as additional age constraints for C012-PC05. All ^{14}C ages were calibrated into calendar ages using the online CALIB 7.1 software (Stuiver et al., 2020) and the Marine20 calibration curve (Heaton et al., 2020). Last appearance datums (LAD) of biostratigraphic indicators *Rouxia leventerae* (last occurrence at MIS 5/6 boundary) and *Hemidiscus karstenii* (last occurrence at MIS 6/7 boundary) were used as additional age constraints when constructing the age model (Bohaty et al., 1998; McKay et al., 2019; Zielinski & Gersonde, 2002) (supporting information Figures S1 and S2).

3. Results

3.1. Visual Descriptions and Physical Properties

At Site C012 the composite depth section revealed an offset of 5 cm in both C012-KC04 and C012-PC05 from C012-MC03. While at Site A005 a 4 cm offset exists between A005-KC02 and A005-PC01 from A005-MC01. From this assessment we assume that any core top loss at both sites is minimal, which we estimate to be approximately 4–5 cm. The new composite depth section generated allowed for comparison of data from multi-, Kasten, and piston cores of similar sites onto one downcore section in cm composite depth (hereafter cmcd).

Both A005-PC01 and C012-PC05 were visually described for their Munsell color and lithology (Figures 3a and 3b). A005-PC01 contains layers of pale yellow (5Y6/3) and green-gray (Gley1/6/10GY) diatom-rich clayey silts separated by gray (Gley1/5/N) and green-gray (Gley1/5/5GY) silty clays. In C012-PC05, similar colors and lithology are observed with the diatom-rich clayey silt layers appearing in yellow-brown (5Y6/4) and gray-brown (2.5Y6/2), which are interspersed with gray (5Y5/2) and brown-gray (5Y6/2) silty clay layers.

The physical property records including MS, NGR and grain size data from both A005-PC01 and C012-PC05 exhibit a cyclic variability downcore that is consistent across all physical data (Figures 3a and 3b). Sections of high MS (>100 SI units $\times 10^5$) are associated with high NGR (>60 cps) and high clay ($>50\%$) content. While sections of low MS and low NG coincide with high silt ($>50\%$) content. In C012-PC05, many of the spikes in MS align with spikes in the coarse grained fraction (300–2 mm wt%), which appear consistently in the high MS, silty clay layers.

The elemental Ba/Al ratios derived from XRF scanning reveal sections of high Ba/Al (>10) that are aligned with low MS and high silt contents in the core (Figures 3a and 3b). Singular deviations from this trend are observed in both piston core records occurring as a spike at 270 cmcd in A005-PC01 and 710 cmcd in C012-PC05, both of which occur during units of high MS and high clay content.

The planktic foraminifera *N. pachyderma* (s) was observed in discrete samples sieved at >63 μm in C012-PC05. Qualitatively, these microfossils are found in highest abundance (>100 specimens) between 255 and 295 cmcd and are common (~ 10 – 100 specimens) to rare (<10 specimens) down to ~ 800 cmcd. Below 800 cmcd, no planktic foraminifera were seen. Visual inspections of foraminifera indicate that the quality of carbonate preservation is best within the sections of high MS, high NGR, and high clay content, while signs of partial dissolution are seen in specimens in diatom-rich interbeds.

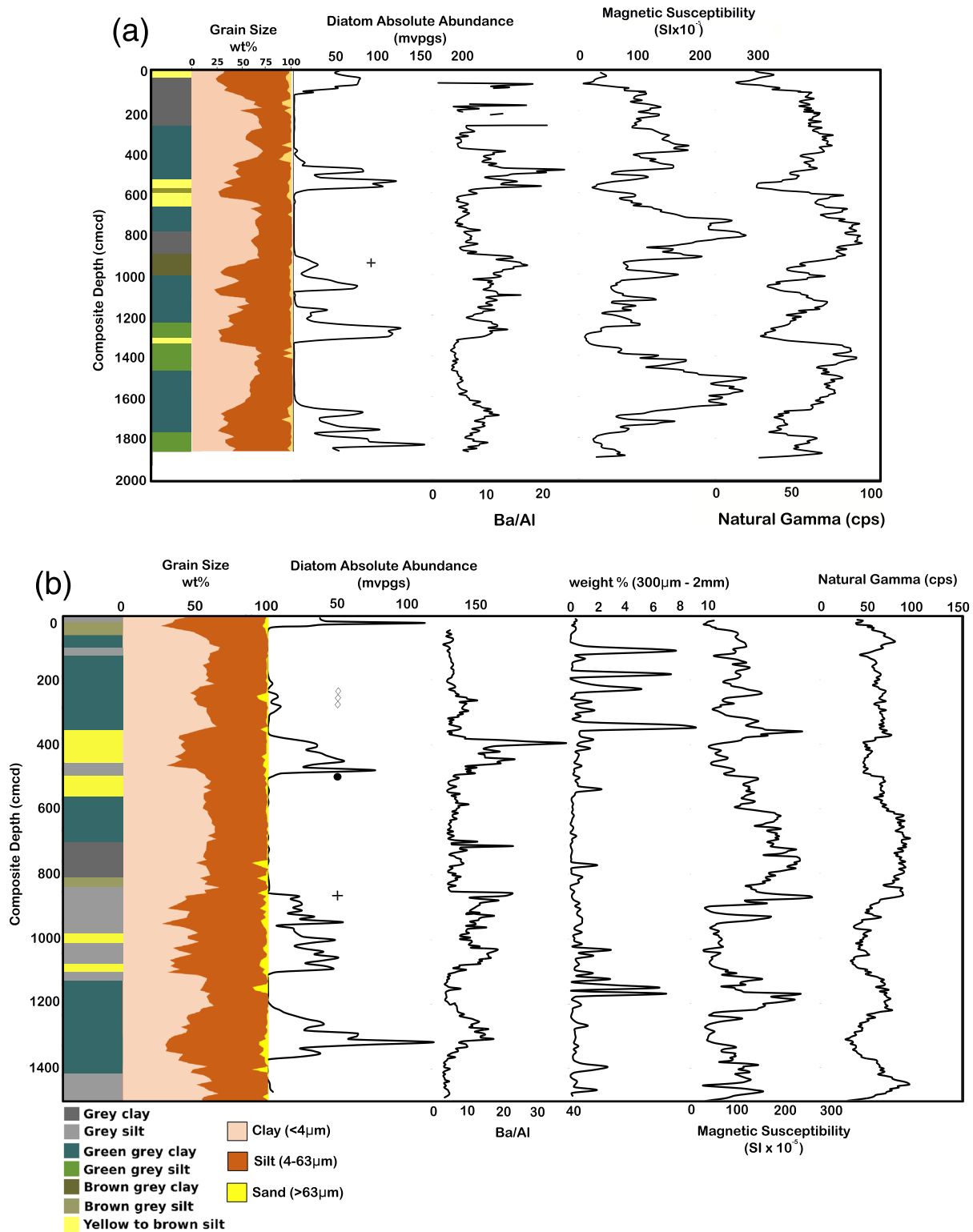


Figure 3. Compiled downcore results from (a) A005-PC01 and (b) C012-PC05 including (from L-R) visual color, grain size %, diatom absolute abundance, Ba/Al ratio, 300–2 mm fraction wt% (only for C012-PC05), magnetic susceptibility, and natural gamma. Absolute age control for C012-PC05 is constrained by calibrated radiocarbon ages (\diamond —range: 34.12 ± 0.55 – 47.87 ± 4.02 cal Kyr BP), the last occurrence of *R. leventerae* (\bullet) and the last occurrence of *H. karstenii* (+). Both sites are displayed against centimeters composite depth (cmcd).

3.2. Diatom Abundances and Assemblages

Diatom absolute abundance is high in intervals of high silt content and Ba/Al, with some samples exceeding 100 million valves per gram of dry sediment (mvpgs) in A005-PC01, C012-PC05, and C012-KC04 (Figures 5–7). The high abundance of whole valves in these intervals suggests that dissolution is not a primary factor influencing assemblage data. Intervals with high MS, NGR, and clay contents contain <2 mvpgs. Diatoms in these intervals are mostly fragmented and generally less well preserved.

The POOZ indicator, *Fragilariopsis kerguelensis* (Crosta et al., 2005), dominates the diatom assemblage throughout both piston cores, contributing 33–88% of the total diatom assemblage. *Thalassiosira lentiginosa*, also a POOZ indicator (Crosta et al., 2005), is subdominant nearly throughout, typically making up 5–15% of the assemblage. *Fragilariopsis kerguelensis* and *T. lentiginosa* exhibit slightly higher relative abundances in biogenic sediments with high diatom absolute abundance than terrigenous sediments. The sea ice indicator *Fragilariopsis curta* (Armand et al., 2005; Gersonde & Zielinski, 2000; Leventer, 1998) is of low relative abundance throughout C012-PC05 with notable contributions (>5%) only in the uppermost 50 cm of the core. *F. curta* is also in low abundance throughout A005-PC01, with contributions >5% only in biogenic intervals. *Chaetoceros* spp. and *Eucampia antarctica* are present in low abundance throughout both cores. *Chaetoceros* spp. are most abundant at the transitions between terrigenous and biogenic intervals. Minor peaks in *Eucampia antarctica* are observed consistently in biogenic sediments compared to terrigenous sediments.

Relative abundance of *Rhizosolenia* spp. and extinct diatoms (*Actinocyclus ingens*, *Denticulopsis* spp. including *Denticulopsis simonsenii*, *Hemidiscus karstenii*, *Rouxia* spp. including *Rouxia leventerae* and *Rouxia constricta*, *Stephanopyxis* spp., *Pyxilla reticulata*) is higher in terrigenous intervals.

3.3. Age Model

The age model for piston core C012-PC05 was developed primarily using planktonic foraminifera *N. pachyderma* (*s*) ^{14}C dates and LAD of diatom biostratigraphic markers (Figure 4). Diatom biostratigraphic indicator species were observed in both piston cores. In C012-PC05, the LAD of *R. leventerae*, associated with the MIS 5/6 boundary, is 540.5 cm, and last occurrence of *H. karstenii*, associated with the MIS 6/7 boundary, is at 920.5 cm (Figure 4). The LAD of *R. leventerae* in C012-PC05 is observed in an interval with low diatom abundance and notable reworking. Therefore, the LAD of *R. leventerae* is interpreted with lower confidence. In A005-PC01, the LAD of *R. leventerae* was unable to be distinguished due to the low diatom absolute abundance and high prevalence of reworked species in MIS 6. The LAD of *H. karstenii* in A005-PC01 was located at 700.5 cm (MIS 6/7 boundary) (Figures 3a and 5). The absence of *H. karstenii* in the low absolute diatom abundance intervals directly overlying the LAD in both cores is not interpreted with complete confidence, since these intervals have extremely low diatom abundances and many of the specimens are reworked. However, the lack of *H. karstenii* in the high diatom abundance interval overlying the LAD, in combination with the differences in absolute diatom abundance, provides support for this pick.

In order to calibrate the radiocarbon samples using the Marine20 calibration curve, an estimate for the regional marine reservoir age (ΔR) was estimated from the core top of the multi-core C012-MC03. The planktonic foraminifera in the C012-MC03 core top were dated to 1080 ± 28 ^{14}C years BP. Assuming that the true age of the core top is 0 year BP, the local *R* value was estimated as 927 ± 31 years BP relative to SHCal20 (Hogg et al., 2020), which agrees closely with modern polar *R* values from the GLODAP database (Key et al., 2004) and supports the assumption that no older reworked carbon is present in the sample. The ΔR value was estimated to be 519 ± 110 years BP from the local *R* value relative to the global average *R* value at 0 year BP in the Marine20 calibration (Heaton et al., 2020). This estimated ΔR value agrees closely with other Southern Ocean ΔR values from the CALIB database determined on mollusk shells from similar depth environments (Berkman & Forman, 1996; Paterne et al., 2019; Sikes & Guilderson, 2016). Additional foraminifera ^{14}C dates in C012-PC05 were obtained from the CaCO_3 -rich bed between 255 and 295 cmcd. Three samples, including the upper and lower contacts of this bed, were dated to show that the bed was deposited during an ~13,000 year interval between 34.12 ± 0.55 to 47.87 ± 4.02 cal. Kyr BP, during MIS 3. The C012-MC03 core top radiocarbon date was used as a constant ΔR correction for these dates when calibrating using the Marine20 calibration (Heaton et al., 2020). While the local *R* value, and hence ΔR value, is expected to vary significantly in polar regions during past glacial phases (Butzin et al., 2005, 2017; Sikes & Guilderson, 2016; Skinner et al., 2010, 2017, 2019), we elect to use a constant ΔR correction for the following reasons. Skinner

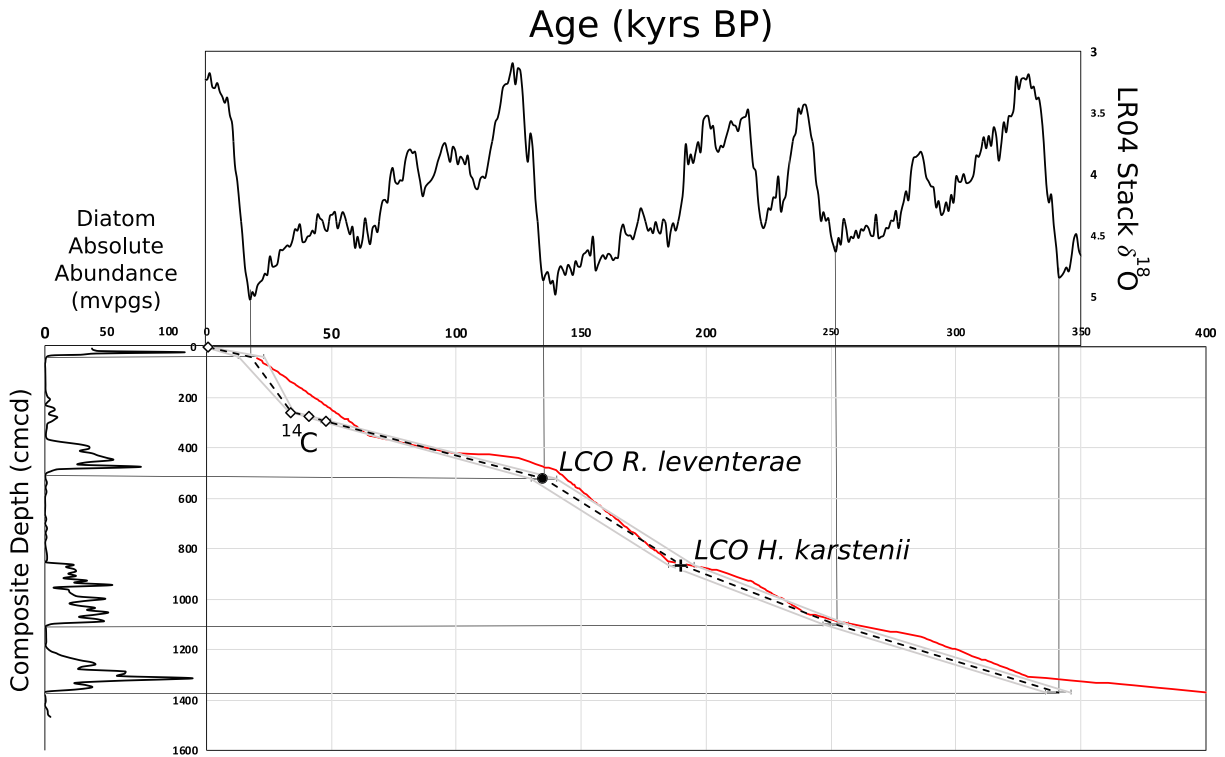


Figure 4. Downcore age model for C012-PC05. Dashed line is the primary age model that incorporates the absolute age control points of foraminiferal radiocarbon dates (\diamond), LCO of *R. leventerae* (\bullet) and *H. karstenii* ($+$) and tie points between the onset of diatom abundance peaks and glacial maxima on the LR04 timescale. Gray line indicates the estimated uncertainty for each tie point. Red line is the secondary age model developed by correlation between the C012-PC05 Ba/Al record to the LR04 timescale (Presti et al., 2011).

et al. (2019) showed that in a compilation of Southern Ocean R value estimates over the last 25 Kyr, the maximum expected change in R value relative to the Holocene is expected during the peak LGM ($\sim 1,000$ years). Taking into account the global average R value from Marine20 at 21 Kyr BP (Heaton et al., 2020), the maximum change in the Southern Ocean ΔR would be ~ 500 years from our Holocene estimate. When the dates in MIS 3 are calibrated with this upper limit in ΔR , the difference in the calibrated and corrected age is $< 1,000$ years. Furthermore, Skinner et al., 2019 showed that the difference in R values relative to the Holocene is seen to temper going back toward MIS 3; hence, the difference in R value for our MIS 3 dates is expected to be less than what was calculated for the LGM upper limit estimate. Finally, the resolution of this age model is only intended to resolve changes on orbital timescales, and hence, while important for higher-resolution age models, it is unnecessary to constrain the sub-millennial variability in polar R values for this purpose.

To improve age control in lower sections of C012-PC05, diatom absolute abundance record was tied to the LR04 benthic $\delta^{18}\text{O}$ stack (Konfirst et al., 2012; Lisiecki & Raymo, 2005). This approach has been used previously on an archive from the continental slope of the Amundsen Sea by Konfirst et al. (2012), who tied peaks in diatom abundance with interglacial maxima from the benthic $\delta^{18}\text{O}$ LR04 stack. Here we elect instead to tie the final point < 10 mvpgs before a diatom abundance peak to an MIS glacial maximum on the LR04 timescale. A similar approach was used by Wilson et al. (2018) to verify the age model of U1361A on the continental rise of Wilkes Land, whereby the lower contact of biogenic intervals was assigned to glacial maxima on the LR04 timescale. The sequence of deglaciation is known to be led by a rapid contraction in perennial sea ice cover, which facilitates primary productivity in surface waters through the availability of light and re-energized nutrient-rich upwelling (Ferrari et al., 2014; Gersonde et al., 2005; Shemesh et al., 2002). Hence, tie points assigned to the glacial terminations correspond with the rapid onset of diatom abundance peaks. We assign an uncertainty of ± 5 Kyr to these tie points to account for differences

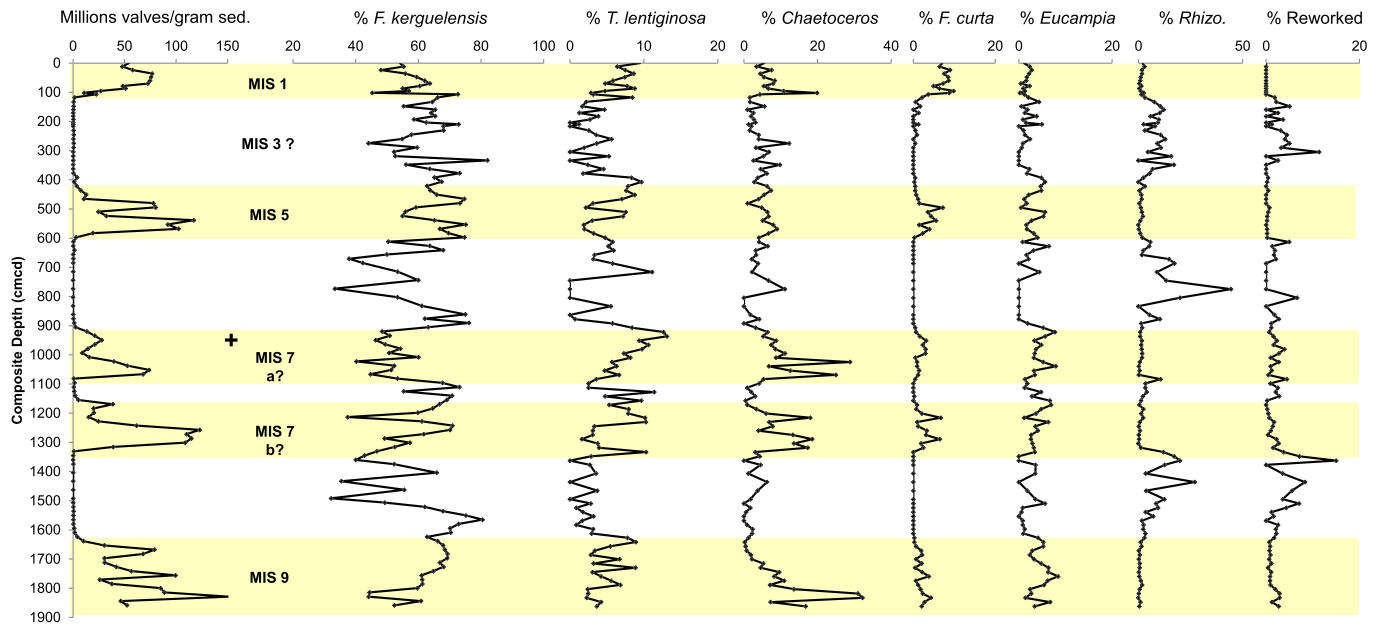


Figure 5. Diatom abundance and assemblages from A005 PC01 including (from L-R) diatom absolute abundance, % *F. kerguelensis*, % *T. lentiginosa*, % *Chaetoceros*, % *F. curta*, % *Rhizosolenia*, and % reworked or extinct diatoms. No official age model was developed for A005-PC01 due to only one absolute age control, the last occurrence of *H. karstenii* (+). Assumed interglacial phases are highlighted in yellow through correlation of peaks in diatom absolute abundance with C012-PC05.

between local changes and the global LR04 timescale. Assuming linear sedimentation from the final tie point, we estimate the age of the base of C012-PC05 as ~380 Kyr. The average sedimentation rate of C012-PC05 calculated from the slope of Figure 4 is 4.6 cmcd/kyr. MIS correlations are supported by the LAD of *H. karstenii* in both A005-PC01 and C012-PC05.

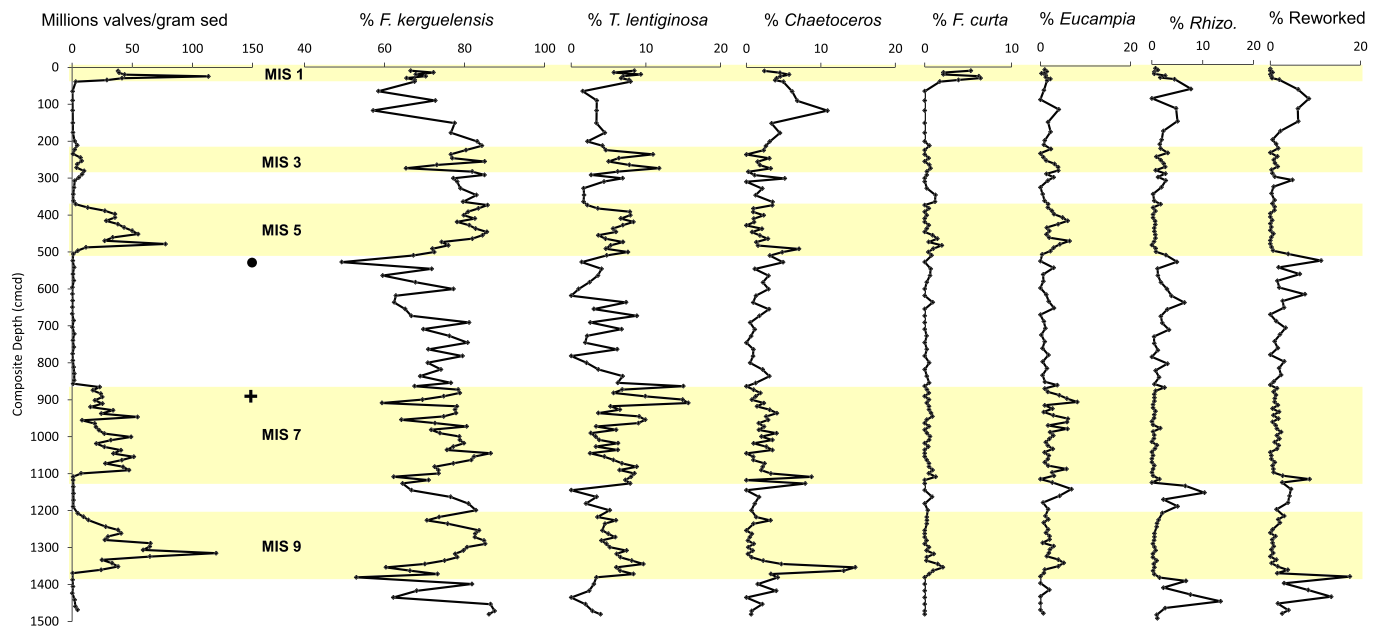


Figure 6. Diatom abundance and assemblages from C012 PC05 including (from L-R) diatom absolute abundance, % *F. kerguelensis*, % *T. lentiginosa*, % *Chaetoceros*, % *F. curta*, % *Rhizosolenia*, and % reworked or extinct diatoms. Interglacial phases highlighted in yellow are based on the age model for C012-PC05 (Figure 4) constrained by calibrated foraminiferal radiocarbon ages and the LCO of *R. leventerae* (●) and *H. karstenii* (+).

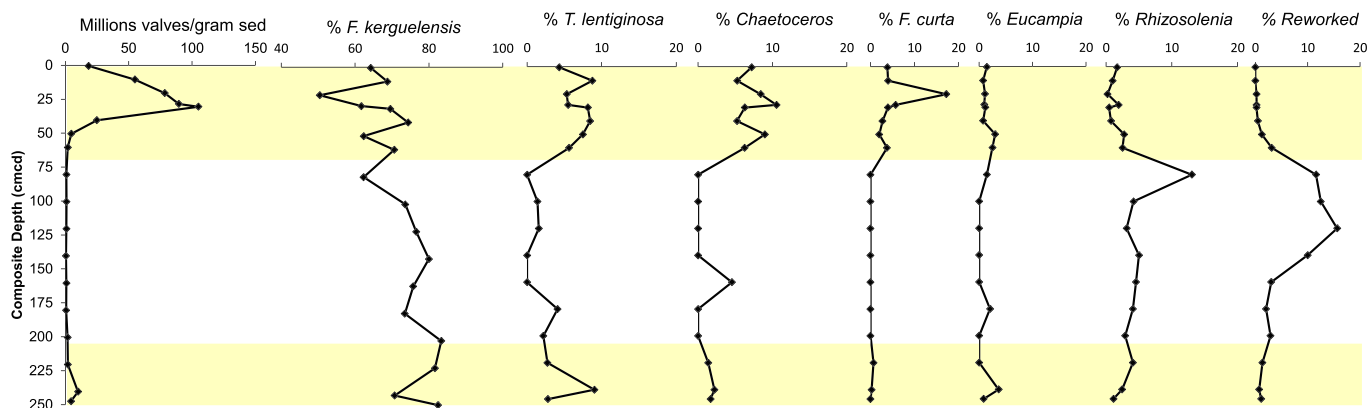


Figure 7. Diatom abundance and assemblages from C012-KC04 including (from L-R) diatom absolute abundance, % *F. kerguelensis*, % *T. lentiginosa*, % *Chaetoceros*, % *F. curta*, % *Rhizosolenia*, and % reworked or extinct diatoms. Interglacials (MIS 1 and 3) are highlighted in yellow from the C012-PC05 age model.

The previous assumption of tying the onset of diatom abundance peaks with glacial terminations on the LR04 timescale was tested by generating a second age model following the methods of Presti et al. (2011) on MD03-2603 from the Wilkes Land continental slope. In this case the C012-PC05 Ba/Al record was correlated with the LR04 benthic $\delta^{18}\text{O}$ stack using the QAnalyseries software to generate ages. Ba/Al ratios have previously been used as a paleoproductivity proxy on the Antarctic margin and exhibit similar cyclic trends to diatom abundance and opal % (Bonn et al., 1998; Hillenbrand et al., 2009; Presti et al., 2011). The two age models (Figure 4) show close agreement with the exception of the period between 18 and 55 Kyr, where the Ba/Al age model deviates from the radiocarbon ages, potentially due to *R* value variability. Based on the close agreement between the two methods, we are confident in our assumption of using the onset of diatom abundance peaks as a tie point for glacial terminations and continue to use this age model for Site C012.

The age model for C012-PC05 shows that units with high MS, high NGR, high clay contents, low Ba/Al, and near-zero diatom abundance correspond to glacial periods MIS 2, 6, 8, and 10. While the units consisting of low MS, low NGR, and high biogenic character inferred from high Ba/Al, high silt and high diatom abundance correspond to interglacial periods MIS 1, 5, 7, and 9. The variations in these properties between glacial and interglacial phases have been previously recognized in other records spanning the middle Pleistocene to Holocene in various of the Antarctic slope sectors including Wilkes Land (Escutia et al., 2003, 2011; Jimenez-Espejo et al., 2020; Presti et al., 2011; Wilson et al., 2018), Dronning Maud Land (Bonn et al., 1998), the Ross Sea (Kim et al., 2020; Ohneiser et al., 2019), Prydz Bay (Passchier et al., 2003; Theissen et al., 2003), and the Antarctic Peninsula (Grobe & Mackensen, 1992; Hillenbrand et al., 2009; Lucchi et al., 2002; Pudsey, 2000).

4. Discussion

4.1. Controls on Slope Sedimentation and Primary Productivity on the Sabrina Coast

The cyclic variability in the data presented in A005-PC01 and C012-PC05 is indicative of different depositional processes acting on the core sites (Figure 8). Here we attribute the variations in the data between glacial and interglacial phases to the primary depositional processes driving them. This reveals clear differences between the primary modes of glacial and interglacial deposition.

4.1.1. Interglacial Phases

Interglacials, as verified by the age model, are inferred in our records to reflect intervals of high diatom abundance, low MS, low NGR, high silt content, and high Ba/Al. Due to the high biogenic content of the sediments, deposition on the slope and rise is driven by the pelagic rain from primary productivity in surface waters. This interpretation is supported by peaks in diatom abundance and high Ba/Al ratios. Ba/Al ratios have also been suggested as an indicator for intense bottom currents since winnowing favors the preservation of heavy minerals such as barite, giving a close correlation with other heavy minerals such as zircon, but this is yet to be shown on the Antarctic margin (Bahr et al., 2014). Peaks in diatom absolute abundance also co-vary with increased accumulation of silts, which, since they were not dissolved from samples

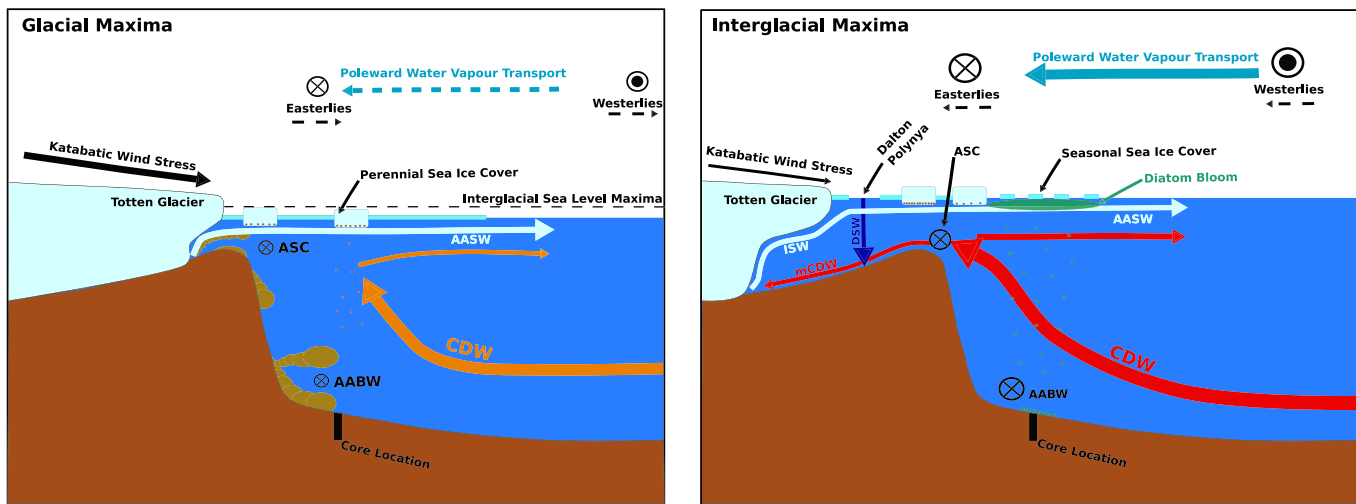


Figure 8. Conceptual schematic (not to scale) highlighting the differences in processes between glacial and interglacial phases (for more examples of schematics from other Antarctic slope locations see Grobe & Mackensen, 1992; Kim et al., 2020; Lucchi et al., 2002; Pudsey, 2000). During glacial maxima an expanded ice sheet advances to the outer shelf reworking sedimentary material toward the shelf break. Sediment gravity flows and sediment laden meltwater plumes and channelized through the gullies on the shelf break and into the canyon networks below. A perennial cover restricts primary productivity and limits hemipelagic sedimentation. Deep water upwelling and the Antarctic wind belts are shifted northward and weakened. During interglacial maxima, the ice sheet retreats onto the inner slope, while the southward shift in the Antarctic wind belt allows deep-water to upwell closer to the shelf and interact with shelf water masses. The larger nutrient availability from deep water and a seasonal sea ice cover allows for high surface primary productivity and biogenic flux to the seafloor.

analyzed for grain size, reflects the high abundance of diatoms in this size fraction. Grain size variations could also be influenced by selective deposition of silt and removal of clay by along-slope bottom currents (McCave & Hall, 2006; Rebesco et al., 2002). Along-slope flows are thought to strengthen during warmer periods due to intensified easterly wind stress driving a stronger ASC (Colleoni et al., 2018; Stewart & Thompson, 2012). Winnowing from an intensified along-slope current is supported by the consistently high sand content during interglacial periods seen at both coring locations. Sand content shows no similarities with the 300–2 mm wt% in C012-PC05, where spikes are seen predominantly during glacials. The relationship between MS and NGR with terrigenous content (Kim et al., 2020; Lee et al., 2017) appears consistent on the Sabrina Coast, where the low MS and NGR during interglacials indicate reduced terrigenous sedimentation at the coring sites. The lithostratigraphic, physical, and diatom abundance observations, inferred to represent interglacial phases, are verified by the foundational body of work developed by multiple ocean drilling legs on sediments from similar time intervals and depositional environments in different sectors of the Antarctic margin. This includes Site 1095 from the Pacific West Antarctic Peninsula sediment drift system (Barker & Camerlenghi, 2002; Barker et al., 1999), Site 1167 from Prydz Bay trough mouth fan (O'Brien et al., 2001; Passchier et al., 2003), Site U1361 from Wilkes Land continental rise (Escutia et al., 2011), and most recently from Sites U1523 and U1524 from the outer continental shelf and lower slope and the Ross Sea (McKay et al., 2019). The common conclusion drawn from this work being is that the characteristics observed in these intervals represent a shift to more ice-distal conditions and sedimentation controlled by hemipelagic deposition under seasonal sea ice conditions.

In combination with the diatom abundance data, the assemblage data support the increased prevalence of open ocean zone conditions during interglacials. This includes increased absolute and relative abundances of *F. kerguelensis* and *T. lentiginosa*, indicating that the summer sea ice edge was south of the study site (Figures 5 and 6). The exception to this trend is MIS 1, where *F. curta* shows a distinct increase, indicating increased prevalence of sea ice associated productivity. However, this is not seen during previous interglacial periods as *F. curta* contributes uniformly low abundances. While dissolution is always a possibility in terms of altering an assemblage, in this case it is less likely to be a primary driver during the intervals with high absolute diatom abundance. The low abundance of sea ice associated taxa during the preceding interglacials is notable and points to the potential influence of oceanic heat flux on sea ice extent. This is further

evidenced by minor peaks in *Eucampia antarctica* relative abundance, which occur most notably in early- and mid-MIS 5 and late-MIS 7 (Figures 5 and 6). Peck et al. (2015) correlate *E. antarctica* abundance with CDW influence due to its association with warm, melt water-stratified conditions (Burckle, 1984; Cremer et al., 2003). Therefore, increased *E. antarctica* abundances may reflect increased oceanic heat flux influence during MIS 5 and 7. Increases in CDW heat flux in regions with a weak slope current, such as the Amundsen Sea, during past warm intervals have been linked with a southward shift of the polar easterly winds and strengthening in the sub-Antarctic westerly winds (Anderson et al., 2009; Obase et al., 2017). Overall, the consistent appearance of diatom abundance maxima throughout each interglacial period since the MPT suggests that the study site was situated within the seasonal sea ice zone. This implies that processes including surface primary productivity, ventilation of upwelling deep water and air-sea exchange of heat and carbon were all active in this region of the East Antarctic.

Chaetoceros subg. *Hyalochaete* show peak relative abundances as diatom absolute abundance begins to increase during glacial terminations and the beginning of interglacials, suggesting an increase in spring blooms in association with deglaciation (Figures 5 and 6). This subgenus is commonly associated with a stable water column and warm, low salinity conditions as is common in the Antarctic Peninsula region (Leventer et al., 2002). Sjunneskog and Taylor (2002) observed high abundances of *Chaetoceros* spp., including *Chaetoceros* resting spores, at the end of the Last Glacial Maximum along the Antarctic Peninsula in association with rapid deglaciation and an increase in open water primary productivity. High abundances of *Chaetoceros* resting spores have also been observed in Prydz Bay following ice shelf retreat (Taylor et al., 1997). Therefore, the *Chaetoceros* subg. *Hyalochaete* peaks observed at Site C012 could be the result of a freshwater input stabilizing the water column during deglaciation. No large peaks in *Chaetoceros* subg. *Hyalochaete* abundance were observed, as have been previously correlated with extreme warming events, such as MIS 31 (Scherer et al., 2008).

Much variability in diatom absolute abundance is observed among interglacials in both A005-PC01 and C012-PC05 (Figures 5 and 6). However, the timing of early versus mid-stage productivity trends is difficult to distinguish due to the low resolution of the age model as well as uncertain variations in sedimentation rates. MIS 1 and 9 both have mid-stage diatom maxima, interpreted as productivity peaks, where diatom absolute abundance more than doubles to >100 mvpgs. Interestingly, while MIS 9 exhibits the strongest peak in diatom absolute abundance, this is accompanied by a more muted peak in Ba/Al in both records. Another discrepancy between the two productivity indicators is seen during MIS 5, which contains an early-stage productivity peak in diatom absolute abundance but a late-stage peak in Ba/Al. While MIS 7 appears to show the closest similarity between diatom absolute abundance and Ba/Al, the peak shapes and timing in A005-PC01 and C012-PC05 are distinctly different. Both archives show generally high diatom absolute abundance and Ba/Al, but in C012-PC05 no noticeable sub-peaks in primary productivity are seen while in A005-PC01 there are two separated peaks with the largest occurring in the early stage. The presence of the interstadial MIS 3 is confirmed in C012-PC05 by radiocarbon dating and coincides with a small peak in diatom abundances and silt content. At Site A005-PC01, MIS 3 is more difficult to determine with the lack of radiocarbon dating. However, a very small peak in diatom abundance and a similar peak in silt content as seen in C012-PC05 are still observed between 300 and 400 cmcd (Figure 5 and supporting information Figure S7) which is likely to be MIS 3.

4.1.2. Glacial Phases

A clear switch in depositional regime during glacial phases is observed in both A005-PC01 and C012-PC03 due to the change to high MS, high NGR, high clay content, low diatom abundance, and low Ba/Al. Deposition of the finer clay fraction along with higher MS and NGR (Figure 9) demonstrates the close relationship between grain size and physical properties and indicates a change in sediment composition whereby terrigenous supply dominates. The high NGR and high clay content co-vary due to the decay of K, Th, and U in clays (De Vleeschouwer et al., 2017). While many of the larger peaks in MS in C012-PC05 align with peaks in the coarse grained 300–2 mm wt%, suggesting higher contents of mafic minerals appear in coarse grained layers (Kim et al., 2020). Low Ba/Al and diatom abundance indicates that primary productivity was severely limited in surface waters with limited light availability from a perennial sea ice cover as the most likely cause (Gersonde et al., 2005). Collins et al. (2012) showed that during the last glaciation (23.5–31 Kyr BP) in the South Atlantic the region of permanent sea ice extended northward by up to 12° latitude possibly as far north as 55°S, which means that during glacials the study site would be south of the

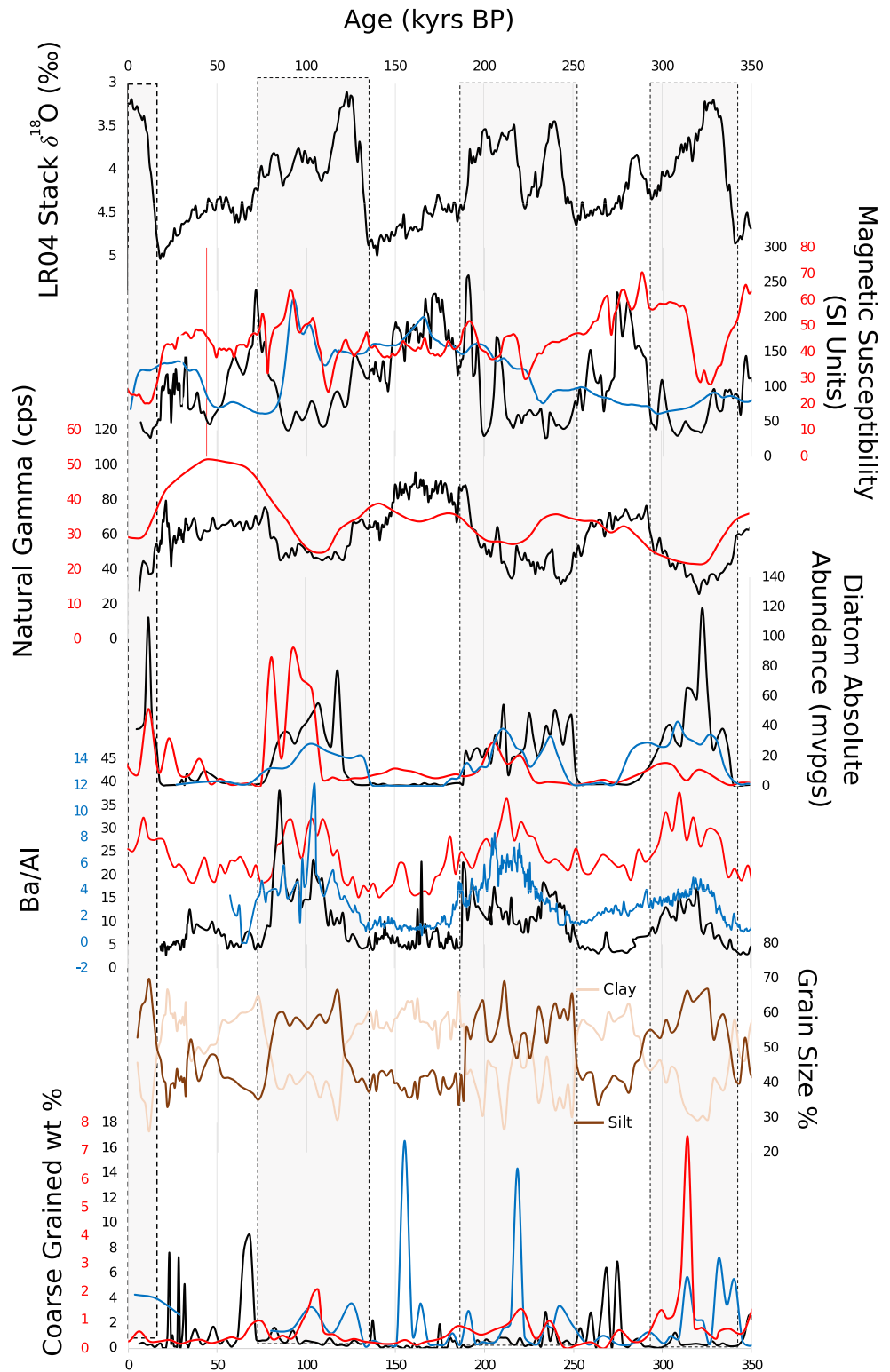


Figure 9. Comparison of Sites C012-PC05 (black) on the Sabrina Coast with IODP site U1361A (red - Escutia et al., 2011; Wilson et al., 2018) from Wilkes Land and PS58/254 (blue—Hillenbrand et al., 2009; Konfirst et al., 2012) from the Amundsen Sea alongside (a) the benthic $\delta^{18}\text{O}$ LR04 stack (Lisiecki & Raymo, 2005), (b) magnetic susceptibility—PS58/254 data on the same axis as C012-PC05, (c) natural gamma, (d) diatom absolute abundance, (e) Ba/Al ratios—U1361 data on the same axis as C012-PC05, (f) clay and silt content—only displayed for C012-PC05, and (g) the coarse grained weight fraction—PS58/254 data on the same axis as C012-PC05.

summer sea ice edge. The smaller spikes in Ba/Al during glacial periods could reflect brief spikes in production that do not show in the diatom abundance data due to poor preservation from thin-walled frustules (Warnock et al., 2015). The 300–2 mm wt%, where peaks are seen to consistently occur during glacials, has been used previously to infer IRD (Cowan et al., 2008; Krissek, 1995; Patterson et al., 2014). There is no indication of grain size fining upward in these layers of high coarse fraction wt%, which are indicative of turbidity deposits; hence, ice rafting is the most likely explanation. Overall, again reinforced by previous observations from ocean drilling legs, the glacial phase indicates a shift to more ice proximal conditions, where sedimentation is dictated by glaciomarine processes and a permanent sea ice cover restricts surface primary productivity.

The glacial depositional interpretation is reinforced by the higher proportion of extinct diatoms and diatoms with robust siliceous frustules (i.e., *Rhizosolenia* spp.) (Figures 5 and 6), which are interpreted as evidence for reworking of older sediments from the continental shelf. The most common reworked diatom species, *Pyxilla reticulata*, last commonly occurs in the late Oligocene (Fenner, 1984; Scherer et al., 2000), indicating that older sediments were exposed, reworked, and delivered to the study site during the Pleistocene. The poor preservation and increased fragmentation of diatoms in these intervals, in combination with the higher relative contribution from extinct taxa, suggest that during glacials, sediments can be both reworked from the previous interglacial population deposited on the shelf and slope and also reworked from the older sedimentary units of the shelf, (Gulick et al., 2017). As *F. kerguelensis* dominates the interglacial diatom assemblages of both A005-PC01 and C012-PC05, they are most likely to be reworked during the advance of the succeeding glacial period. Therefore, dominance of *F. kerguelensis* in the glacial diatom assemblages may reflect previously deposited older material being delivered from the shelf in combination with limited intervals of open water primary productivity. Extinct taxa are considered to be reworked from subcropping sediments.

Glacial intervals on the Antarctic margin are marked by the expansion of the Antarctic Ice Sheet across the continental shelf recorded by the scouring of sedimentary strata on the shelf (Figure 8). On the Sabrina Coast, it is still unknown how far grounded ice advanced toward the shelf break during glaciations since the MPT. However, geophysical surveys of the Sabrina Coast shelf have revealed successive patterns of advance and retreat of grounded ice from the Totten Glacier and Moscow University Ice Shelf (Fernandez et al., 2018; Gulick et al., 2017; Montelli et al., 2019). Fernandez et al. (2018) concluded from seismic profiles and swath bathymetry that grounded ice from the Moscow University Ice Shelf reached 5 km from the shelf break at some point in time. The repeated advance and retreat of grounded ice across the shelf exerts a strong control on sedimentation on the continental slope due to the erosive capacity of the ice sheet on sedimentary strata (Mackintosh et al., 2014; Prothro et al., 2018). Advance of grounded ice across the shelf reworks sediment into grounding zone wedges where sediment is bulldozed toward the shelf break (Fernandez et al., 2018; Post et al., 2020). Along the upper slope, gullies with low-slope angles trigger sediment failure, resulting in sediment gravity flows that are funneled through the canyon network seen next to Site C012 (Post et al., 2020). The fine fraction of the flow settles slowly and is lofted to the west of canyon systems by along-slope currents such as the westward flowing ASC and AABW (O'Brien et al., 2020). The increase in terrigenous sedimentation at the study site during glacial periods most likely relates to more frequent occurrence of sediment gravity flows from sediment loading along the shelf break.

Downslope sediment gravity flows and reworking from along-slope currents have been a consistent feature in molding channel-levee systems around the Antarctic margin during cooler periods (Escutia et al., 2002). In the eastern region, seaward of the Moscow University Ice Shelf, sediment routing is focused by the gullies along the shelf break (Post et al., 2020) and funneled into the Maadjit and Manang canyons whereby the fine fraction is lofted across the ridgeline to Site C012 (Close, 2010; O'Brien et al., 2020). This depositional system is thought to be very similar to Site U1361 and others along canyon-ridge networks off Wilkes Land (Escutia et al., 2003, 2011; Jimenez-Espejo et al., 2020; Presti et al., 2011). Terrigenous input to the western region of the study location at Site A005 differs from the east. This environment is thought to share similarities with the sediment drifts formed along the Antarctic Margin (Barker & Camerlenghi, 2002; Rebesco et al., 1996). The broader canyon morphology of the Minang-a canyon adjacent to the larger and shallower ridge suggests that it is not fed frequently by sediment gravity flows from the shelf (O'Brien et al., 2020) where instead terrigenous material accumulates in response to along-slope currents associated with

AABW farther to the east. Kim et al. (2020) proposed that along-slope transport associated with the ASC strengthened during past glacial periods as evidenced by enhanced winnowing of fine grained material in glacial sediments on the Iselin Bank in the Ross Sea sector. The higher clay content during glacials appears to go against this conclusion; however, direct grain size comparison between the records is difficult due to different methods and more importantly different depth environments with the shallower cores in Kim et al. (2020) likely to be more significantly influenced by the ASC (McKay et al., 2019). Despite these differences in depositional environment between locations, both A005-PC01 and C012-PC05 exhibit very similar patterns of terrigenous input—high during glacials and low during interglacials (Figure 8). This similarity indicates that processes including downslope sediment gravity flows and along-slope contouritic deposition were the primary modes of deposition during this time.

Sea ice exerts an equally important control on sedimentation by limiting surface primary productivity (Arrigo et al., 2008). The dearth of diatoms in glacial sediments from A005-PC01 and C012-PC05 indicates that permanent summer sea ice conditions extended past their modern limit during glaciations since the MPT. This agrees with previous studies based on modeling (Ferrari et al., 2014) and a circum-Antarctic observations of diatom abundances and assemblages (Benz et al., 2016; Collins et al., 2012; Gersonde et al., 2005; Ghadi et al., 2020) and other proxy compilations (Fischer et al., 2010; Kohfeld & Chase, 2017), which suggests a northward advance of 10–12° latitude in the permanent summer sea ice edge during past glacial periods. During such glacial intervals, permanent sea ice cover impacts the spatial distribution and extent of primary productivity in the upper ocean, influencing the diatom record at the sea floor (Armand, 2000; Armand & Leventer, 2009). However, more importantly, an extended permanent summer sea ice cover is thought to have a significant influence on deep ocean circulation (Ferrari et al., 2014) and the global carbon cycle (Fischer et al., 2010; Stephens & Keeling, 2000). The physical barrier formed by permanent sea ice restricts air-sea gas exchange and CO₂ outgassing, while also stratifying surface waters during summer melt and hence restricting the ventilation of deep water (Collins et al., 2012). Ghadi et al., 2020 reported a northward shift in the seasonal winter sea ice extent to 49°S in the Indian sector of the Southern Ocean during the last glacial period. This study adds further constraint to the permanent summer sea ice extent, which must have extended north of 64°S during glaciations since the MPT. The implications of this, as described in Ferrari et al. (2014), are a homogenized water column at the study location comprised of deep waters entirely of Antarctic origin, with incorporation of warmer northern sourced waters restricted to regions north of the permanent summer sea ice extent (Marzocchi & Jansen, 2019; Wilson et al., 2020).

4.2. Comparison With Other Middle Pleistocene to Holocene Antarctic Slope Records

The similarity in trends across all properties examined in A005-PC01 and C012-PC05 warrants comparison with other Antarctic slope records spanning the middle Pleistocene to Holocene (Figure 9). The data presented in this paper from C012-PC05 are compared with data from Hole U1361A (3,454 m water depth) from Wilkes Land (Escutia et al., 2011; Wilson et al., 2018) and from site PS58/254 (4,014 m water depth) from the Amundsen Sea Embayment (Hillenbrand et al., 2009; Konfirst et al., 2012). Both records are located in similar depositional environments (Dowdeswell et al., 2006; Escutia et al., 2003) and are seaward of marine-terminating outlet glaciers that are vulnerable to intrusions of CDW (Fretwell et al., 2013; Thoma et al., 2008). We note that recorded data density and sedimentation rates differ between sites and between glacial-interglacial periods, which creates temporal aliasing. The average linear sedimentation rates for C012-PC05, U1361A, and PS58/254 are 4.6, 1.7, and 2.0 cm/kyr, respectively, for the last 300 kyr.

The similarities between diatom abundance records at each location and peak abundance occur during interglacial periods followed by near-zero abundance during glacial periods, again relate to variations in the permanent and seasonal extent of sea ice in each sector (Figure 9d). This first confirms that during glaciations since the MPT, the extent of permanent sea ice extended north the Antarctic slope and rise, isolating the Antarctic Ice Sheet from warmer northern sourced waters and restricting air-sea gas exchange, which could account for the majority of the glacial drop in atmospheric CO₂ (Kohfeld & Chase, 2017; Marzocchi & Jansen, 2019; Stephens & Keeling, 2000). Second, the interglacial shift to seasonal sea ice cover confirms that productivity in each sector was enhanced along with upwelling of warmer nutrient-rich northern sourced deep waters (Anderson et al., 2009). However, the larger peaks in diatom abundance in C012-PC05 during MIS 1 and 9 stand out compared with the other records, highlighting that productivity can vary significantly between each sector due to nutrient availability and/or sea ice cover. Diatom

abundance, NGR, and Ba/Al ratios appear to be a faithful recorder of glacial-interglacial cycles due to their close relationship with the benthic $\delta^{18}\text{O}$ LR04 stack (Figures 9c and 9e; Hillenbrand et al., 2009; Konfirst et al., 2012). However, if these records are to be used to provide secondary age control, tie points should not be drawn between peaks since our comparison shows that local processes influence the timing of these maxima. Most of the variability in the Ba/Al record can be accounted for by changes in diatom absolute abundance, confirming that it is primarily a productivity indicator in each sector (Bonn et al., 1998). However, slight differences between Ba/Al and diatom absolute abundance in the timing of maxima values could indicate that current speeds also influence this proxy particularly during warmer interglacials when the strength of the ASC is thought to be enhanced (Bahr et al., 2014; Colleoni et al., 2018). The most variation between records is seen in the MS data which, because of its relationship with grain size, is most likely to be influenced by local processes such as sediment gravity flows and ice rafting that confound the glacial-interglacial signal (Figures 9b and 9g). This can be seen in the similarity between peaks in MS and the coarse-grained wt%. At Wilkes Land there is also a close relationship between peaks in the IRD inferred coarse-grained wt% and shifts in detrital provenance to more inland terrains showing that an ice sheet response can be linked with IRD peaks and MS trends (Wilson et al., 2018). While in the Amundsen Sea record, which also exhibits prominent IRD peaks during MIS 5 and 9, the vulnerability of the West Antarctic Ice Sheet through the Pine Island Basin is linked with the advection of CDW onto the shelf, modulated by the Amundsen Sea Low (Thoma et al., 2008).

From the Sabrina Coast data set presented herein, we cannot make inferences about the dynamics of the EAIS or the intrusion of CDW onto the shelf during interglacials since the MPT. However, the consistency of observations in lithostratigraphy, diatom absolute abundance, Ba/Al, NGR, and in some cases MS in slope sediments around the Antarctic margin indicates that the fundamental processes governing sedimentation during glacials and interglacials have not changed significantly since the MPT. While differences in the intensity and duration of glacials and interglacials may be influenced by differences in insolation (Yin & Berger, 2015), the clear distinction between sedimentation regimes between glacials and interglacials outlined in this paper relates to the high-amplitude swings in climate characteristic to post-MPT glacial cycles (Jouzel et al., 2007). Central to this are increased variability in Antarctic ice sheet volume, Southern Ocean SST, and sea ice extent (Clark et al., 2006; McClymont et al., 2013), which exert primary controls on sedimentation along the Antarctic slope environment. These processes in turn also influence the redistribution of deep ocean water masses, which deliver heat closer to or further from the ice sheet and influence grounding line stability (Colleoni et al., 2018; Ferrari et al., 2014).

5. Conclusions

Sedimentary archives retrieved from the Sabrina Coast continental slope and rise document the history of sediment accumulation in channel-levee complexes seaward of the Totten Glacier. An age model constructed on C012-PC05 based on radiocarbon dating of foraminifera, biostratigraphic datums, and diatom abundance correlated with the LR04 benthic $\delta^{18}\text{O}$ stack indicates that the sedimentary sequence covers multiple glacial cycles since the MPT. Physical properties, grain size analysis, Ba/Al, and diatom abundance data show a clear cyclic pattern between glacial and interglacial phases. Glacial periods are defined by higher terrigenous input to the site from sediment gravity flows and along-slope currents as evidenced by high clay content, NGR and MS. The low diatom abundance also seen in glacial intervals indicates that permanent summer sea ice extended across the slope at least north of 64°S. Interglacials are defined by high biogenic sedimentation from enhanced primary productivity facilitated by a seasonal winter sea ice cover, evidenced by high diatom abundances and Ba/Al ratios. Variability in the sedimentary records is seen between and among glacials and interglacials with respect to differences in sediment routing from the shelf to the two sites. Comparison with other slope records from Wilkes Land and the Amundsen Sea spanning the same time period shows that the observed patterns of variability in lithostratigraphy, diatom abundance, Ba/Al, and physical properties are common to different regions of the Antarctic. The implications being that the primary processes controlling sedimentation on the Antarctic slope environment being the movement of grounded ice across the shelf and the extent of sea ice coverage have been continuously active during the high-amplitude glacial cycles since the MPT. This research establishes a framework for future paleoceanographic work on these sites and with improved spatial coverage from other records that will elucidate further insights into past ocean-ice sheet interactions along the Sabrina Coast.

Data Availability Statement

Data can be accessed on request of the authors at the following doi links: diatom data for A005-PC01 and C012-PC05 (doi:10.26179/5cad45a7cb140) (Leventer, 2020) and physical property data including MS, natural gamma, and sedimentation rates for A005-PC01 and C012-PC03 (<https://doi.org/10.25919/5ebcccf5d13ca>) (Holder et al., 2020). The MS and Natural Gamma data should be attributed to the following: Dimitrios Evangelinos, Adrián López Quirós, Philip O'Brien, Leanne Armand, the Marine National Facility, and the CSIRO. Grain size analysis for A005-PC01 and C012-PC03 <http://dbforms.ga.gov.au/pls/www/npm.mars.search> at *Interactions of the Totten Glacier through multiple glacial cycles*; visual logs for A005-PC01 and C012-PC03 at 10.25911/5e96e309b1fea and 10.25911/5e96e303cdfdb (O'Brien et al., 2020a, 2020b); XRF data for A005-PC01 and C012-PC03 at doi:10.26179/5e97d91f0771e (O'Brien & Opdyke, 2020).

Acknowledgments

We thank the Marine National Facility, the IN2017-V01 scientific party-led by the Chief Scientists L. K. Armand and P. O'Brien, and MNF support staff and ASP crew members led by Capt. M. Watson for their help and support on board the *RV Investigator*. Isabel Dove and Meaghan Kendall contributed to the diatom work. We wish to thank the Associate Editor and three anonymous reviewers for their valuable and constructive comments that greatly improved this manuscript. This Project is supported through funding from the Australian Government's Australian Antarctic Science Grant Program (AAS 4333) and by the Australian Government through the Australian Research Council (DP170100557). Additional funding was provided by the National Science Foundation Antarctic Integrated Systems Science Project (grants PLR-1143836).

References

- Alves, E. Q., Macario, K. D., Urrutia, F. P., Cardoso, R. P., & Bronk Ramsey, C. (2019). Accounting for the marine reservoir effect in radiocarbon calibration. *Quaternary Science Reviews*, 209, 129–138. <https://doi.org/10.1016/j.quascirev.2019.02.013>
- Anderson, J. B., Brake, C. F., & Myers, N. C. (1984). Sedimentation on the Ross Sea continental shelf, Antarctica. *Marine Geology*, 57(1–4), 295–333. [https://doi.org/10.1016/0025-3227\(84\)90203-2](https://doi.org/10.1016/0025-3227(84)90203-2)
- Anderson, J. B., Conway, H., Bart, P. J., Witus, A. E., Greenwood, S. L., McKay, R. M., et al. (2014). Ross Sea paleo-ice sheet drainage and deglacial history during and since the LGM. *Quaternary Science Reviews*, 100, 31–54. <https://doi.org/10.1016/j.quascirev.2013.08.020>
- Anderson, R. F., Ali, S., Bradtmiller, L. I., Nielsen, S. H. H., Fleisher, M. Q., Anderson, B. E., & Burckle, L. H. (2009). Wind-driven upwelling in the Southern Ocean and the deglacial rise in atmospheric CO₂. *Science*, 323(5920), 1443 LP–1448. <https://doi.org/10.1126/science.1167441>
- Armand, L. (2000). An ocean of ice—Advances in the estimation of past sea ice in the Southern Ocean. *GSA Today*, 10, 1–7.
- Armand, L. K., Crosta, X., Romero, O., & Pichon, J.-J. (2005). The biogeography of major diatom taxa in Southern Ocean sediments. *Palaeogeography, Palaeoclimatology, Palaeoecology*, 223(1–2), 93–126. <https://doi.org/10.1016/j.palaeo.2005.02.015>
- Armand, L. K., & Leventer, A. (2009). Palaeo sea ice distribution and reconstruction derived from the geological record. In *Sea Ice* (pp. 469–529). Chichester, UK: Wiley-Blackwell. <https://doi.org/10.1002/9781444317145.ch13>
- Armand, L., O'Brien, P., & On-board Scientific Party (2018). Interactions of the Totten Glacier with the Southern Ocean through multiple glacial cycles (IN2017-V01): Post-survey report. Canberra: Research School of Earth Sciences, Australian National University. Retrieved from <http://hdl.handle.net/1885/142525>
- Arndt, J. E., Schenke, H. W., Jakobsson, M., Nitsche, F. O., Buys, G., Goleby, B., et al. (2013). The international bathymetric chart of the Southern Ocean (IBCSO) version 1.0—A new bathymetric compilation covering circum-Antarctic waters. *Geophysical Research Letters*, 40, 3111–3117. <https://doi.org/10.1002/grl.50413>
- Arrigo, K. R., van Dijken, G. L., & Bushinsky, S. (2008). Primary production in the Southern Ocean, 1997–2006. *Journal of Geophysical Research*, 113, C08004. <https://doi.org/10.1029/2007JC004551>
- Bahr, A., Jiménez-Espejo, F. J., Kolasinac, N., Grunert, P., Hernández-Molina, F. J., Röhl, U., et al. (2014). Deciphering bottom current velocity and paleoclimate signals from contourite deposits in the Gulf of Cádiz during the last 140 kyr: An inorganic geochemical approach. *Geochemistry, Geophysics, Geosystems*, 15, 3145–3160. <https://doi.org/10.1002/2014GC005356>
- Barker, P. F., & Camerlenghi, A. (2002). Glacial history of the Antarctic peninsula from Pacific margin sediments. In P. F. Barker, A. Camerlenghi, G. D. Acton, A. T. S. Ramsay (Eds.), *Proc. ODP, Sci. Results* (Vol. 178, pp. 1–40). College Station, TX: Ocean Drilling Program. <https://doi.org/10.2973/odp.proc.sr.178.238.2002>
- Barker, P. F., Camerlenghi, A., Acton, G. D., & Shipboard Scientific Party (1999). *Proc. ODP, Init. Repts* (Vol. 178). College Station, TX: Ocean Drilling Program. <https://doi.org/10.2973/odp.proc.ir.178.1999>
- Basak, C., Fröllje, H., Lamy, F., Gersonde, R., Benz, V., Anderson, R. F., et al. (2018). Breakup of last glacial deep stratification in the South Pacific. *Science*, 359(6378), 900 LP–904. Retrieved from <http://science.sciencemag.org/content/359/6378/900.abstract>
- Benz, V., Esper, O., Gersonde, R., Lamy, F., & Tiedemann, R. (2016). Last glacial maximum sea surface temperature and sea-ice extent in the Pacific sector of the Southern Ocean. *Quaternary Science Reviews*, 146, 216–237. <https://doi.org/10.1016/j.quascirev.2016.06.006>
- Berkman, P. A., & Forman, S. L. (1996). Pre-bomb radiocarbon and the reservoir correction for calcareous marine species in the Southern Ocean. *Geophysical Research Letters*, 23(4), 363–366. Retrieved from <https://www.scopus.com/inward/record.uri?eid=2-s2.0-0029769043%26partnerID=40%26md5=0f5dd0e1ce1ced5a14f69faa38ef22b5>, <https://doi.org/10.1029/96GL00151>
- Bindoff, N. L., Rosenberg, M. A., & Warner, M. J. (2000). On the circulation and water masses over the Antarctic continental slope and rise between 80 and 150°E. *Deep-Sea Research Part II: Topical Studies in Oceanography*. [https://doi.org/10.1016/S0967-0645\(00\)00038-2](https://doi.org/10.1016/S0967-0645(00)00038-2)
- Bohaty, S., Scherer, R., & Harwood, D. M. (1998). Quaternary diatom biostratigraphy and palaeoenvironments of the CRP-1 drillcore, Ross Sea, Antarctica. *Terra Antarctica*, 5(3), 431–453.
- Bonn, W. J., Ginge, F. X., Grobe, H., Mackensen, A., & Fütterer, D. K. (1998). Palaeoproductivity at the Antarctic continental margin: Opal and barium records for the last 400 ka. *Palaeogeography, Palaeoclimatology, Palaeoecology*, 139(3), 195–211. [https://doi.org/10.1016/S0031-0182\(97\)00144-2](https://doi.org/10.1016/S0031-0182(97)00144-2)
- Burckle, L. H. (1984). Diatom distribution and paleoceanographic reconstruction in the Southern Ocean—Present and Last Glacial Maximum. *Marine Micropaleontology*, 9(3), 241–261.
- Butzin, M., Köhler, P., & Lohmann, G. (2017). Marine radiocarbon reservoir age simulations for the past 50,000 years. *Geophysical Research Letters*, 44, 8473–8480. <https://doi.org/10.1002/2017GL074688>
- Butzin, M., Prange, M., & Lohmann, G. (2005). Radiocarbon simulations for the glacial ocean: The effects of wind stress, Southern Ocean sea ice and Heinrich events. *Earth and Planetary Science Letters*, 235(1), 45–61. <https://doi.org/10.1016/j.epsl.2005.03.003>
- Caburlotto, A., Lucchi, R. G., de Santis, L., Macri, P., & Tolotti, R. (2010). Sedimentary processes on the Wilkes Land continental rise reflect changes in glacial dynamic and bottom water flow. *International Journal of Earth Sciences*. <https://doi.org/10.1007/s00531-009-0422-8>

- Ceccaroni, L., Frank, M., Frignani, M., Langone, L., Ravaioli, M., & Mangini, A. (1998). Late Quaternary fluctuations of biogenic component fluxes on the continental slope of the Ross Sea, Antarctica. *Journal of Marine Systems*, *17*(1–4), 515–525. [https://doi.org/10.1016/S0924-7963\(98\)00061-X](https://doi.org/10.1016/S0924-7963(98)00061-X)
- Cefarelli, A. O., Ferrario, M. E., Almandoz, G. O., Atencio, A. G., Akselman, R., & Vernet, M. (2010). Diversity of the diatom genus *Fragilariopsis* in the Argentine Sea and Antarctic waters: Morphology, distribution and abundance. *Polar Biology*, *33*(11), 1463–1484. <https://doi.org/10.1007/s00300-010-0794-z>
- Clark, P. U., Archer, D., Pollard, D., Blum, J. D., Rial, J. A., Brovkin, V., et al. (2006). The middle Pleistocene transition: Characteristics, mechanisms, and implications for long-term changes in atmospheric pCO₂. *Quaternary Science Reviews*, *25*(23–24), 3150–3184. <https://doi.org/10.1016/j.quascirev.2006.07.008>
- Close, D. I. (2010). Slope and fan deposition in deep-water turbidite systems, East Antarctica. *Marine Geology*, *274*(1), 21–31.
- Close, D. I., Stagg, H. M. J., & O'Brien, P. E. (2007). Seismic stratigraphy and sediment distribution on the Wilkes Land and Terre Adélie margins, East Antarctica. *Marine Geology*, *239*(1–2), 33–57. <https://doi.org/10.1016/j.margeo.2006.12.010>
- Cody, R. D., Levy, R. H., Harwood, D. M., & Sadler, P. M. (2008). Thinking outside the zone: High-resolution quantitative diatom biochronology for the Antarctic Neogene. *Palaeogeography, Palaeoclimatology, Palaeoecology*, *260*(1–2), 92–121. <https://doi.org/10.1016/j.palaeo.2007.08.020>
- Colleoni, F., De Santis, L., Siddoway, C. S., Bergamasco, A., Golledge, N. R., Lohmann, G., et al. (2018). Spatio-temporal variability of processes across Antarctic ice-bed-ocean interfaces. *Nature Communications*, *9*(1), 2289. <https://doi.org/10.1038/s41467-018-04583-0>
- Collins, L. G., Hounslow, M. W., Allen, C. S., Hodgson, D. A., Pike, J., & Karloukovski, V. V. (2012). Palaeomagnetic and biostratigraphic dating of marine sediments from the Scotia Sea, Antarctica: First identification of the Laschamp excursion in the Southern Ocean. *Quaternary Geochronology*, *7*, 67–75. <https://doi.org/10.1016/j.quageo.2011.10.002>
- Cowan, E. A., Hillenbrand, C.-D., Hassler, L. E., & Ake, M. T. (2008). Coarse-grained terrigenous sediment deposition on continental rise drifts: A record of Plio-Pleistocene glaciation on the Antarctic peninsula. *Palaeogeography, Palaeoclimatology, Palaeoecology*, *265*(3–4), 275–291. <https://doi.org/10.1016/J.PALAEO.2008.03.010>
- Cremer, H., Gore, D., Melles, M., & Roberts, D. (2003). Palaeoclimatic significance of late Quaternary diatom assemblages from southern Windmill Islands, East Antarctica. *Palaeogeography, Palaeoclimatology, Palaeoecology*, *195*(3–4), 261–280.
- Crosta, X., Romero, O., Armand, L. K., & Pichon, J.-J. (2005). The biogeography of major diatom taxa in Southern Ocean sediments: 2. Open ocean related species. *Palaeogeography, Palaeoclimatology, Palaeoecology*, *223*(1–2), 66–92. <https://doi.org/10.1016/J.PALAEO.2005.03.028>
- De Vleeschouwer, D., Dunlea, A. G., Auer, G., Anderson, C. H., Brumsack, H., de Loach, A., et al. (2017). Quantifying K, U, and Th contents of marine sediments using shipboard natural gamma radiation spectra measured on DV JOIDES resolution. *Geochemistry, Geophysics, Geosystems*, *18*, 1053–1064. <https://doi.org/10.1002/2016GC006715>
- DeConto, R. M., & Pollard, D. (2016). Contribution of Antarctica to past and future sea-level rise. *Nature*, *531*(7596), 591–597. <https://doi.org/10.1038/nature17145>
- Domack, E., Duran, D., Leventer, A., Ishman, S., Doane, S., McCallum, S., et al. (2005). Stability of the Larsen B ice shelf on the Antarctic Peninsula during the Holocene epoch. *Nature*, *436*(7051), 681–685. <https://doi.org/10.1038/nature03908>
- Domack, E., O'Brien, P., Harris, P., Taylor, F., Quilty, P. G., De Santis, L., & Raker, B. (1998). Late Quaternary sediment facies in Prydz Bay, East Antarctica and their relationship to glacial advance onto the continental shelf. *Antarctic Science*, *10*(3), 236–246.
- Donda, F., Brancolini, G., O'Brien, P., Santis, L., & Escutia, C. (2007). Sedimentary processes in the Wilkes Land margin: A record of the Cenozoic east Antarctic ice sheet evolution. *Journal of The Geological Society - J GEOL SOC*, *164*(1), 243–256. <https://doi.org/10.1144/0016-76492004-159>
- Dowdeswell, J. A., Evans, J., Ó Cofaigh, C., & Anderson, J. B. (2006). Morphology and sedimentary processes on the continental slope off Pine Island Bay, Amundsen Sea, West Antarctica. *GSA Bulletin*, *118*(5–6), 606–619. <https://doi.org/10.1130/B25791.1>
- Dutton, A., Carlson, A. E., Long, A. J., Milne, G. A., Clark, P. U., DeConto, R., et al. (2015). Sea-level rise due to polar ice-sheet mass loss during past warm periods. *Science*, *349*(6244). Retrieved from. <http://science.sciencemag.org/content/349/6244/aaa4019.abstract>, <https://doi.org/10.1126/science.aaa4019>
- Escutia, C., Brinkhuis, H., Klaus, A., & the IODP Expedition 318 Scientists (2011). IODP expedition 318: From greenhouse to icehouse at the Wilkes Land Antarctic margin. *Scientific Drilling*, *12*, 15–23. <https://doi.org/10.2204/iodp.sd.12.02.2011>
- Escutia, C., Eitrem, S. L., Cooper, A. K., & Nelson, C. H. (2000). Morphology and acoustic character of the Antarctic Wilkes Land turbidite systems: Ice-sheet-sourced versus river-sourced fans. *Journal of Sedimentary Research*, *70*(1), 84–93. <https://doi.org/10.1306/2DC40900-0E47-11D7-8643000102C1865D>
- Escutia, C., Nelson, C. H., Acton, G. D., Eitrem, S. L., Cooper, A. K., Warnke, D. A., & Jaramillo, J. M. (2002). Current controlled deposition on the Wilkes Land continental rise, Antarctica. *Geological Society, London, Memoirs*, *22*(1), 373. Retrieved from. <http://mem.lyellcollection.org/content/22/1/373.abstract>
- Escutia, C., Warnke, D., Acton, G. D., Barcena, A., Burckle, L., Canals, M., & Frazee, C. S. (2003). Sediment distribution and sedimentary processes across the Antarctic Wilkes Land margin during the quaternary. *Deep Sea Research Part II: Topical Studies in Oceanography*, *50*(8–9), 1481–1508. [https://doi.org/10.1016/S0967-0645\(03\)00073-0](https://doi.org/10.1016/S0967-0645(03)00073-0)
- Fallon, S. J., Fifield, L. K., & Chappell, J. M. (2010). The next chapter in radiocarbon dating at the Australian National University: Status report on the single stage AMS. *Nuclear Instruments and Methods in Physics Research, Section B: Beam Interactions with Materials and Atoms*, *268*(7–8), 898–901. <https://doi.org/10.1016/j.nimb.2009.10.059>
- Fenner, J. (1984). Eocene-Oligocene planktic diatom stratigraphy in the low latitudes and the high southern latitudes. *Micropaleontology*, *30*(4), 319–342. <https://doi.org/10.2307/1485708>
- Fernandez, R., Gulick, S., Domack, E., Montelli, S., Leventer, A., Shevenell, A., & Frederick, B. (2018). Past ice stream and ice sheet changes on the continental shelf off the Sabrina Coast, East Antarctica. *Geomorphology*. <https://doi.org/10.1016/j.geomorph.2018.05.020>
- Ferrari, R., Jansen, M. F., Adkins, J. F., Burke, A., Stewart, A. L., & Thompson, A. F. (2014). Antarctic sea ice control on ocean circulation in present and glacial climates. *Proceedings of the National Academy of Sciences*, *111*(24), 8753 LP–8758. <https://doi.org/10.1073/pnas.1323922111>
- Fischer, H., Schmitt, J., Lüthi, D., Stocker, T. F., Tschumi, T., Parekh, P., et al. (2010). The role of Southern Ocean processes in orbital and millennial CO₂ variations—A synthesis. *Quaternary Science Reviews*, *29*(1–2), 193–205. <https://doi.org/10.1016/j.quascirev.2009.06.007>
- Flament, T., & Rémy, F. (2012). Dynamic thinning of Antarctic glaciers from along-track repeat radar altimetry. *Journal of Glaciology*, *58*(211), 830–840. <https://doi.org/10.3189/2012JoG11J118>
- Fretwell, P., Pritchard, H. D., Vaughan, D. G., Bamber, J. L., Barrand, N. E., Bell, R., et al. (2013). Bedmap2: Improved ice bed, surface and thickness datasets for Antarctica. *The Cryosphere*, *7*(1), 375–393. <https://doi.org/10.5194/tc-7-375-2013>

- Gersonde, R., Crosta, X., Abelmann, A., & Armand, L. (2005). Sea-surface temperature and sea ice distribution of the Southern Ocean at the EPILOG Last Glacial Maximum—A circum-Antarctic view based on siliceous microfossil records. *Quaternary Science Reviews*, *24*(7–9), 869–896. <https://doi.org/10.1016/J.QUASCIREV.2004.07.015>
- Gersonde, R., & Zielinski, U. (2000). The reconstruction of late Quaternary Antarctic sea-ice distribution—The use of diatoms as a proxy for sea-ice. *Palaeogeography, Palaeoclimatology, Palaeoecology*, *162*(3–4), 263–286. [https://doi.org/10.1016/S0031-0182\(00\)00131-0](https://doi.org/10.1016/S0031-0182(00)00131-0)
- Ghadi, P., Nair, A., Crosta, X., Mohan, R., Manoj, M. C., & Melo, T. (2020). Antarctic sea-ice and paleoproductivity variation over the last 156,000 years in the Indian sector of Southern Ocean. *Marine Micropaleontology*, *160*, 101894. <https://doi.org/10.1016/j.marmicro.2020.101894>
- Golledge, N. R., Fogwill, C. J., Mackintosh, A. N., & Buckley, K. M. (2012). Dynamics of the last glacial maximum Antarctic ice-sheet and its response to ocean forcing. *Proceedings of the National Academy of Sciences*, *109*(40), 16052 LP–16056. <https://doi.org/10.1073/pnas.1205385109>
- Greenbaum, J. S., Blankenship, D. D., Young, D. A., Richter, T. G., Roberts, J. L., Aitken, A. R. A., et al. (2015). Ocean access to a cavity beneath Totten Glacier in East Antarctica. *Nature Geoscience*, *8*(4), 294–298. <https://doi.org/10.1038/ngeo2388>
- Greene, C. A., Blankenship, D. D., Gwyther, D. E., Silvano, A., & Van Wijk, E. (2017). Wind causes Totten ice shelf melt and acceleration. *Science Advances*, *3*(11). <https://doi.org/10.1126/sciadv.1701681>
- Grobe, H., & Mackensen, A. (1992). Late Quaternary climatic cycles as recorded in sediments from the Antarctic continental margin. In *The Antarctic paleoenvironment: A perspective on global change: Part one* (pp. 349–376). Washington, DC: American Geophysical Union.
- Gulick, S. P. S., Shevenell, A. E., Montelli, A., Fernandez, R., Smith, C., Warny, S., et al. (2017). Initiation and long-term instability of the east Antarctic ice sheet. *Nature*, *552*(7684), 225–229. <https://doi.org/10.1038/nature25026>
- Heaton, T. J., Köhler, P., Butzin, M., Bard, E., Reimer, R. W., Austin, W. E. N., et al. (2020). Marine20—The marine radiocarbon age calibration curve (0–55,000 cal BP). *Radiocarbon*, *62*(4), 779–820. <https://doi.org/10.1017/RDC.2020.68>
- Hillenbrand, C.-D., Kuhn, G., & Frederichs, T. (2009). Record of a mid-Pleistocene depositional anomaly in west Antarctic continental margin sediments: An indicator for ice-sheet collapse? *Quaternary Science Reviews*, *28*(13), 1147–1159. <https://doi.org/10.1016/j.quascirev.2008.12.010>
- Hogg, A. G., Heaton, T. J., Hua, Q., Palmer, J. G., Turney, C. S. M., Southon, J., et al. (2020). SHCal20 southern hemisphere calibration, 0–55,000 years cal BP. *Radiocarbon*, *62*(4), 759–778. <https://doi.org/10.1017/RDC.2020.59>
- Holder, L., Duffy, M., Opdyke, B., Leventer, A., Post, A., O'Brien, P., & Armand, L. (2020). RV Investigator IN2017_V01 two piston core records from the East Antarctic Sabrina Coast region. *Marine National Facility; CSIRO*. Retrieved from <https://data.csiro.au/collections/collection/Cicsiro:43057v7/DItrue>
- Jimenez-Espejo, F. J., Presti, M., Kuhn, G., McKay, R., Crosta, X., Escutia, C., et al. (2020). Late Pleistocene oceanographic and depositional variations along the Wilkes Land margin (East Antarctica) reconstructed with geochemical proxies in deep-sea sediments. *Global and Planetary Change*, *184*, 103045. <https://doi.org/10.1016/J.GLOPLACHA.2019.103045>
- Jouzel, J., Masson-Delmotte, V., Cattani, O., Dreyfus, G., Falourd, S., Hoffmann, G., et al. (2007). Orbital and millennial Antarctic climate variability over the past 800,000 years. *Science*, *317*(5839), 793–796. <https://doi.org/10.1126/science.1141038>
- Key, R. M., Kozyr, A., Sabine, C. L., Lee, K., Wanninkhof, R., Bullister, J. L., et al. (2004). A global ocean carbon climatology: Results from global data analysis project (GLODAP). *Global Biogeochemical Cycles*, *18*, GB4031. <https://doi.org/10.1029/2004GB002247>
- Kim, S., Lee, J. I., McKay, R. M., Yoo, K.-C., Bak, Y.-S., Lee, M. K., et al. (2020). Late pleistocene paleoceanographic changes in the Ross Sea—Glacial-interglacial variations in paleoproductivity, nutrient utilization, and deep-water formation. *Quaternary Science Reviews*, *239*, 106356. <https://doi.org/10.1016/j.quascirev.2020.106356>
- Kohfeld, K. E., & Chase, Z. (2017). Temporal evolution of mechanisms controlling ocean carbon uptake during the last glacial cycle. *Earth and Planetary Science Letters*, *472*, 206–215. <https://doi.org/10.1016/j.epsl.2017.05.015>
- Kohfeld, K. E., Graham, R. M., De Boer, A. M., Sime, L. C., Wolff, E. W., Le Quéré, C., & Bopp, L. (2013). Southern hemisphere westerly wind changes during the Last Glacial Maximum: Paleo-data synthesis. *Quaternary Science Reviews*, *68*, 76–95.
- Konfirst, M. A., Scherer, R. P., Hillenbrand, C.-D., & Kuhn, G. (2012). A marine diatom record from the Amundsen Sea—Insights into oceanographic and climatic response to the mid-Pleistocene transition in the west Antarctic sector of the Southern Ocean. *Marine Micropaleontology*, *92–93*, 40–51. <https://doi.org/10.1016/j.marmicro.2012.05.001>
- Kopp, R. E., Simons, F. J., Mitrovica, J. X., Maloof, A. C., & Oppenheimer, M. (2009). Probabilistic assessment of sea level during the last interglacial stage. *Nature*, *462*(7275), 863–867. http://www.nature.com/nature/journal/v462/n7275/supinfo/nature08686_S1.html
- Kotov, S., & Pälke, H. (2018). QAnalyze—A cross-platform time series tuning and analysis tool. AGU Fall meeting, <https://agu.confex.com/agu/fm18/meetingapp.cgi/Paper/349843>
- Krissek, L. A. (1995). Late Cenozoic ice-rafting records from leg 145 sites in the North Pacific: Late Miocene onset, late Pliocene intensification, and Plio-Pleistocene events. *Proceeding of the Ocean Drilling Program, Scientific Results*, *145*, 179–194.
- Lee, J. I., Yoon, H. I., Yoo, K.-C., Lim, H. S., Lee, Y. I., Kim, D., et al. (2017). Late Quaternary glacial–interglacial variations in sediment supply in the southern Drake Passage. *Quaternary Research*, *78*(1), 119–129. <https://doi.org/10.1016/j.yqres.2012.03.010>
- Leventer, A. (1998). The fate of Antarctic “sea ice diatoms” and their use as paleoenvironmental indicators. In *Antarctic sea ice: Biological processes, interactions and variability* (pp. 121–137). Washington, DC: American Geophysical Union. <https://doi.org/10.1029/AR073p0121>
- Leventer, A. (2020). Quantitative Diatom data collected from the 2017 RV Investigator voyage, IN2017_V01_C022_KC11. *Australian Antarctic Data Centre*. https://data.aad.gov.au/metadata/records/AAS_4333_IN2017_V01_C022_KC11_Diatom_Data
- Leventer, A., Domack, E., Barkoukis, A., McAndrews, B., & Murray, J. (2002). Laminations from the Palmer deep: A diatom-based interpretation. *Paleoceanography*, *17*(3), 8002. <https://doi.org/10.1029/2001PA000624>
- Li, X., Rignot, E., Morlighem, M., Mouginot, J., & Scheuchl, B. (2015). Grounding line retreat of Totten Glacier, East Antarctica, 1996 to 2013. *Geophysical Research Letters*, *42*, 8049–8056. <https://doi.org/10.1002/2015GL065701>
- Lisiecki, L. E., & Raymo, M. E. (2005). A Pliocene–Pleistocene stack of 57 globally distributed benthic delta O-18 records. *Paleoceanography*, *20*, PA1003. <https://doi.org/10.1029/2004PA001071>
- Lucchi, R. G., Rebesco, M., Camerlenghi, A., Busetti, M., Tomadin, L., Villa, G., et al. (2002). Mid-late Pleistocene glacial marine sedimentary processes of a high-latitude, deep-sea sediment drift (Antarctic Peninsula Pacific margin). *Marine Geology*, *189*(3–4), 343–370. [https://doi.org/10.1016/S0025-3227\(02\)00470-X](https://doi.org/10.1016/S0025-3227(02)00470-X)
- Lüthi, D., Le Floch, M., Bereiter, B., Blunier, T., Barnola, J.-M., Siegenthaler, U., et al. (2008). High-resolution carbon dioxide concentration record 650,000–800,000 years before present. *Nature*, *453*(7193), 379. Retrieved from <https://doi.org/10.1038/nature06949>
- Mackintosh, A. N., Verleyen, E., O'Brien, P. E., White, D. A., Jones, R. S., McKay, R., et al. (2014). Retreat history of the East Antarctic Ice Sheet since the Last Glacial Maximum. *Quaternary Science Reviews*, *100*, 10–30. <https://doi.org/10.1016/j.quascirev.2013.07.024>

- Marzocchi, A., & Jansen, M. F. (2019). Global cooling linked to increased glacial carbon storage via changes in Antarctic sea ice. *Nature Geoscience*, *12*(12), 1001–1005. <https://doi.org/10.1038/s41561-019-0466-8>
- Matsumoto, K., Lynch-Stieglitz, J., & Anderson, R. F. (2001). Similar glacial and Holocene Southern Ocean hydrography. *Paleoceanography*, *16*(5), 445–454. <https://doi.org/10.1029/2000PA000549>
- McCave, I. N., Crowhurst, S. J., Kuhn, G., Hillenbrand, C.-D., & Meredith, M. P. (2014). Minimal change in Antarctic Circumpolar Current flow speed between the last glacial and Holocene. *Nature Geoscience*, *7*(2), 113–116. <https://doi.org/10.1038/ngeo2037>
- McCave, I. N., & Hall, I. R. (2006). Size sorting in marine muds: Processes, pitfalls, and prospects for paleoflow-speed proxies. *Geochemistry, Geophysics, Geosystems*, *7*, QION05. <https://doi.org/10.1029/2006GC001284>
- McClymont, E. L., Sosdian, S. M., Rosell-Melé, A., & Rosenthal, Y. (2013). Pleistocene sea-surface temperature evolution: Early cooling, delayed glacial intensification, and implications for the mid-Pleistocene climate transition. *Earth-Science Reviews*, *123*, 173–193.
- McKay, R. M., de Santis, L., Kulhanek, D. K., Ash, J. L., Beny, F., Browne, I. M., et al. (2019). Expedition 374 summary. In R. M. McKay, L. de Santis, D. K. Kulhanek, the Expedition 374 Scientists (Eds.), *Ross Sea West Antarctic ice sheet history, Proceedings of the International Ocean Discovery Program* (Vol. 374, pp. 1–41). College Station, TX: International Ocean Discovery Program. <https://doi.org/10.14379/iodp.proc.374.101.2019>
- Montelli, A., Gulick, S. P. S., Fernandez, R., Frederick, B. C., Shevenell, A. E., Leventer, A., & Blankenship, D. D. (2019). Seismic stratigraphy of the Sabrina Coast shelf, East Antarctica: Early history of dynamic meltwater-rich glaciations. *GSA Bulletin*, *132*(3–4), 545–561. <https://doi.org/10.1130/B35100.1>
- Nitsche, F. O., Porter, D., Williams, G., Cougnon, E. A., Fraser, A. D., Correia, R., & Guerrero, R. (2017). Bathymetric control of warm ocean water access along the East Antarctic Margin. *Geophysical Research Letters*, *44*, 8936–8944. <https://doi.org/10.1002/2017GL074433>
- O'Brien, P., & Opdyke, B. (2020). Piston Core Xray Florescence (XRF) scan data off the Totten Glacier, Sabrina Coast Antarctica. *Australian Antarctic Data Centre*. Retrieved from https://data.aad.gov.au/metadata/records/AAS_4333_core_XRF
- O'Brien, P., Opdyke, B., Post, A., & Armand, L. (2020a). Sabrina Sea Floor Survey (IN2017-V01) Piston Core Images, Visual Logs and grain size DATA summaries IN2017-V01-A005-PC01. *ANU Research Publications*. <https://openresearch-repository.anu.edu.au/handle/1885/202963>
- O'Brien, P., Opdyke, B., Post, A., & Armand, L. (2020b). Sabrina Sea Floor Survey (IN2017-V01) Piston Core Images, Visual Logs and Grain Size Data Summaries IN2017-V01-C012-PC05. *ANU Research Publications*. <https://openresearch-repository.anu.edu.au/handle/1885/202962>
- O'Brien, P. E., Cooper, A. K., Richter, C., & Shipboard Scientific Party (2001). *Proc. ODP, Init. Repts* (Vol. 188). College Station, TX: Ocean Drilling Program. <https://doi.org/10.2973/odp.proc.ir.188.2001>
- O'Brien, P. E., Post, A. L., Edwards, S., Martin, T., Caburlotto, A., Donda, F., et al. (2020). Continental slope and rise geomorphology seaward of the Totten Glacier, East Antarctica (112°E–122°E). *Marine Geology*, *427*. <https://doi.org/10.1016/j.margeo.2020.106221>
- Obase, T., Abe-Ouchi, A., Kushara, K., Hasumi, H., & Ohgaito, R. (2017). Responses of basal melting of Antarctic ice shelves to the climatic forcing of the Last Glacial Maximum and CO₂ doubling. *Journal of Climate*, *30*(10), 3473–3497. <https://doi.org/10.1175/JCLI-D-15-0908.1>
- Ohneiser, C., Yoo, K.-C., Albot, O. B., Cortese, G., Riesselman, C., Lee, J. I., et al. (2019). Magneto-biostratigraphic age models for Pleistocene sedimentary records from the Ross Sea. *Global and Planetary Change*, *176*, 36–49. <https://doi.org/10.1016/j.gloplacha.2019.02.013>
- Orsi, A. H., Whitworth Iii, T., & Nowlin, W. D. Jr. (1995). On the meridional extent and fronts of the Antarctic Circumpolar Current. *Deep-Sea Research Part I*, *42*(5), 641–673. [https://doi.org/10.1016/0967-0637\(95\)00021-W](https://doi.org/10.1016/0967-0637(95)00021-W)
- Passchier, S., O'Brien, P. E., Damuth, J. E., Januszczak, N., Handwerger, D. A., & Whitehead, J. M. (2003). Pliocene–Pleistocene glacio-marine sedimentation in eastern Prydz Bay and development of the Prydz trough-mouth fan, ODP sites 1166 and 1167, East Antarctica. *Marine Geology*, *199*(3–4), 279–305.
- Paterne, M., Michel, E., & Héros, V. (2019). Variability of marine ¹⁴C reservoir ages in the Southern Ocean highlighting circulation changes between 1910 and 1950. *Earth and Planetary Science Letters*, *511*, 99–104. <https://doi.org/10.1016/j.epsl.2019.01.029>
- Patterson, M. O., McKay, R., Naish, T., Escutia, C., Jimenez-Espejo, F. J., Raymo, M. E., et al. (2014). Orbital forcing of the East Antarctic ice sheet during the Pliocene and Early Pleistocene. *Nature Geoscience*, *7*(11), 841–847. <https://doi.org/10.1038/ngeo2273>
- Peck, V. L., Allen, C. S., Kender, S., McClymont, E. L., & Hodgson, D. A. (2015). Oceanographic variability on the West Antarctic Peninsula during the Holocene and the influence of upper circumpolar deep water. *Quaternary Science Reviews*, *119*, 54–65. <https://doi.org/10.1016/J.QUASCIREV.2015.04.002>
- Peña-Molino, B., McCartney, M. S., & Rintoul, S. R. (2016). Direct observations of the Antarctic Slope Current transport at 113° E. *Journal of Geophysical Research: Oceans*, *121*, 7390–7407. <https://doi.org/10.1002/2015JC011594>
- Pollard, D., DeConto, R. M., & Alley, R. B. (2015). Potential Antarctic Ice Sheet retreat driven by hydrofracturing and ice cliff failure. *Earth and Planetary Science Letters*, *412*, 112–121.
- Post, A. L., O'Brien, P. E., Edwards, S., Carroll, A. G., Malakoff, K., & Armand, L. K. (2020). Upper slope processes and seafloor ecosystems on the Sabrina continental slope, East Antarctica. *Marine Geology*, *422*, 106091. <https://doi.org/10.1016/j.margeo.2019.106091>
- Presti, M., Barbara, L., Denis, D., Schmidt, S., De Santis, L., & Crosta, X. (2011). Sediment delivery and depositional patterns off Adélie Land (East Antarctica) in relation to late Quaternary climatic cycles. *Marine Geology*, *284*(1–4), 96–113. <https://doi.org/10.1016/j.margeo.2011.03.012>
- Prothro, L. O., Simkins, L. M., Majewski, W., & Anderson, J. B. (2018). Glacial retreat patterns and processes determined from integrated sedimentology and geomorphology records. *Marine Geology*, *395*, 104–119. <https://doi.org/10.1016/j.margeo.2017.09.012>
- Pudsey, C. J. (2000). Sedimentation on the continental rise west of the Antarctic Peninsula over the last three glacial cycles. *Marine Geology*, *167*(3–4), 313–338. [https://doi.org/10.1016/S0025-3227\(00\)00039-6](https://doi.org/10.1016/S0025-3227(00)00039-6)
- Raymo, M. E., Lisiecki, L. E., & Nisancioglu, K. H. (2006). Plio-pleistocene ice volume, Antarctic climate, and the global delta O-18 record. *Science*, *313*(5786), 492–495. <https://doi.org/10.1126/science.1123296>
- Raymo, M. E., & Mitrovica, J. X. (2012). Collapse of polar ice sheets during the stage 11 interglacial. *Nature*, *483*(7390), 453–456. <http://www.nature.com/nature/journal/v483/n7390/abs/nature10891.html#supplementary-information>, <https://doi.org/10.1038/nature10891>
- Rebesco, M., Larter, R. D., Camerlenghi, A., & Barker, P. F. (1996). Giant sediment drifts on the continental rise west of the Antarctic Peninsula. *Geo-Marine Letters*, *16*(2), 65–75.
- Rebesco, M., Pudsey, C. J., Canals, M., Camerlenghi, A., Barker, P. F., Estrada, F., & Giorgetti, A. (2002). Sediment drifts and deep-sea channel systems, Antarctic Peninsula Pacific Margin. *Geological Society, London, Memoirs*, *22*(1), 353 LP–371. <https://doi.org/10.1144/GSL.MEM.2002.022.01.25>

- Rebesco, M., Hernández-Molina, F. J., Van Rooij, D., & Wåhlin, A. (2014). Contourites and associated sediments controlled by deep-water circulation processes: State-of-the-art and future considerations. *Marine Geology*, *352*, 111–154. <https://doi.org/10.1016/J.MARGEO.2014.03.011>
- Reimer, P. J., Austin, W. E. N., Bard, E., Bayliss, A., Blackwell, P. G., Bronk Ramsey, C., et al. (2020). The IntCal20 northern hemisphere radiocarbon age calibration curve (0–55 cal kBP). *Radiocarbon*, *62*(4), 725–757. <https://doi.org/10.1017/RDC.2020.41>
- Rignot, E., Mouginit, J., Scheuchl, B., van den Broeke, M., van Wessem, M. J., & Morlighem, M. (2019). Four decades of Antarctic Ice Sheet mass balance from 1979–2017. *Proceedings of the National Academy of Sciences*, *116*(4), 1095–1103.
- Rintoul, S. R. (1985). On the origin and influence of Adélie land bottom water. *Ocean, Ice, and Atmosphere: Interactions at the Antarctic Continental Margin*, *75*, 151–171.
- Rintoul, S. R., Silvano, A., Pena-Molino, B., van Wijk, E., Rosenberg, M., Greenbaum, J. S., & Blankenship, D. D. (2016). Ocean heat drives rapid basal melt of the Totten Ice Shelf. *Science Advances*, *2*(12), e1601610. <https://doi.org/10.1126/sciadv.1601610>
- Roberts, J. L., Warner, R. C., Young, D., Wright, A., van Ommen, T. D., Blankenship, D. D., et al. (2011). Refined broad-scale sub-glacial morphology of Aurora Subglacial Basin, East Antarctica derived by an ice-dynamics-based interpolation scheme. *The Cryosphere*, *5*(3), 551–560. <https://doi.org/10.5194/tc-5-551-2011>
- Scherer, R., Bohaty, S. M., & Harwood, D. (2000). Oligocene and lower Miocene siliceous microfossil biostratigraphy of Cape Roberts project core CRP-2/2A, Victoria Land Basin, Antarctica. *Terra Antarctica*, *7*.
- Scherer, R. P., Bohaty, S. M., Dunbar, R. B., Esper, O., Flores, J.-A., Gersonde, R., et al. (2008). Antarctic records of precession-paced insolation-driven warming during early Pleistocene Marine Isotope Stage 31. *Geophysical Research Letters*, *35*, L03505. <https://doi.org/10.1029/2007GL032254>
- Shemesh, A., Hodell, D., Crosta, X., Kanfoush, S., Charles, C., & Guilderson, T. (2002). Sequence of events during the last deglaciation in Southern Ocean sediments and Antarctic ice cores. *Paleoceanography*, *17*(4), 1056. <https://doi.org/10.1029/2000PA000599>
- Sikes, E. L., & Guilderson, T. P. (2016). Southwest Pacific Ocean surface reservoir ages since the last glaciation: Circulation insights from multiple-core studies. *Paleoceanography*, *31*, 298–310. <https://doi.org/10.1002/2015PA002855>
- Silvano, A., Rintoul, S. R., Peña-Molino, B., & Williams, G. D. (2017). Distribution of water masses and meltwater on the continental shelf near the Totten and Moscow University ice shelves. *Journal of Geophysical Research: Oceans*, *122*, 2050–2068. <https://doi.org/10.1002/2016JC012115>
- Sime, L. C., Kohfeld, K. E., Le Quéré, C., Wolff, E. W., de Boer, A. M., Graham, R. M., & Bopp, L. (2013). Southern hemisphere westerly wind changes during the Last Glacial Maximum: Model-data comparison. *Quaternary Science Reviews*, *64*, 104–120.
- Sjunneskog, C., & Taylor, F. (2002). Postglacial marine diatom record of the Palmer deep, Antarctic Peninsula (ODP leg 178, site 1098) 1. Total diatom abundance. *Paleoceanography*, *17*(3), 8803. <https://doi.org/10.1029/2000PA000563>
- Skinner, L. C., Fallon, S., Waelbroeck, C., Michel, E., & Barker, S. (2010). Ventilation of the deep Southern Ocean and deglacial CO₂ rise. *Science*, *328*(5982), 1147. Retrieved from <http://science.sciencemag.org/content/328/5982/1147/abstract>
- Skinner, L. C., Muschitiello, F., & Scrivner, A. E. (2019). Marine reservoir age variability over the last deglaciation: Implications for marine carbon cycling and prospects for regional radiocarbon calibrations. *Paleoceanography and Paleoclimatology*, *34*, 1807–1815. <https://doi.org/10.1029/2019PA003667>
- Skinner, L. C., Primeau, F., Freeman, E., de la Fuente, M., Goodwin, P. A., Gottschalk, J., et al. (2017). Radiocarbon constraints on the glacial ocean circulation and its impact on atmospheric CO₂. *Nature Communications*, *8*(1), 1–10.
- Spence, P., Holmes, R. M., Hogg, A. M., Griffies, S. M., Stewart, K. D., & England, M. H. (2017). Localized rapid warming of West Antarctic subsurface waters by remote winds. *Nature Clim. Change, advance on*. <https://doi.org/10.1038/nclimate3335http://www.nature.com/nclimate/journal/vaop/ncurrent/abs/nclimate3335.html#supplementary-information>
- Stagg, H. M. J., Colwel, J. B., Direen, N. G., O'Brien, P. E., Bernardel, G., Borissova, I., et al. (2004). Geology of the Continental Margin of Enderby and Mac. Robertson Lands, East Antarctica: Insights from a Regional Data Set. *Marine Geophysical Researches*, *25*(3–4), 183–219. <https://doi.org/10.1007/s11001-005-1316-1>
- Stephens, B. B., & Keeling, R. F. (2000). The influence of Antarctic Sea ice on glacial–interglacial CO₂ variations. *Nature*, *404*(6774), 171–174. <https://doi.org/10.1038/35004556>
- Stewart, A. L., & Thompson, A. F. (2012). Sensitivity of the ocean's deep overturning circulation to easterly Antarctic winds. *Geophysical Research Letters*, *39*, L18604. <https://doi.org/10.1029/2012GL053099>
- Stuiver, M., Reimer, P. J., & Reimer, R. W. (2020). CALIB 7.1 [WWW program]. Retrieved from <http://calib.org>
- Tamura, T., Ohshima, K. I., & Nihashi, S. (2008). Mapping of sea ice production for Antarctic coastal polynyas. *Geophysical Research Letters*, *35*, L07606. <https://doi.org/10.1029/2007GL032903>
- Tan, X., Liu, F., Hu, L., Reed, A. H., Furukawa, Y., & Zhang, G. (2017). Evaluation of the particle sizes of four clay minerals. *Applied Clay Science*, *135*, 313–324. <https://doi.org/10.1016/j.clay.2016.10.012>
- Taylor, F., McMinn, A., & Franklin, D. (1997). Distribution of diatoms in surface sediments of Prydz Bay, Antarctica. *Marine Micropaleontology*, *32*(3–4), 209–229. [https://doi.org/10.1016/S0377-8398\(97\)00021-2](https://doi.org/10.1016/S0377-8398(97)00021-2)
- Theissen, K. M., Dunbar, R. B., Cooper, A. K., Mucciarone, D. A., & Hoffmann, D. (2003). The Pleistocene evolution of the East Antarctic Ice Sheet in the Prydz bay region: Stable isotopic evidence from ODP Site 1167. *Global and Planetary Change*, *39*(3–4), 227–256. [https://doi.org/10.1016/S0921-8181\(03\)00118-8](https://doi.org/10.1016/S0921-8181(03)00118-8)
- Thoma, M., Jenkins, A., Holland, D., & Jacobs, S. (2008). Modelling Circumpolar Deep Water intrusions on the Amundsen Sea continental shelf, Antarctica. *Geophysical Research Letters*, *35*, L18602. <https://doi.org/10.1029/2008GL034939>
- Thompson, A. F., Stewart, A. L., Spence, P., & Heywood, K. J. (2018). The Antarctic slope current in a changing climate. *Reviews of Geophysics*, *56*, 741–770. <https://doi.org/10.1029/2018RG000624>
- Toggweiler, J. R., & Russell, J. (2008). Ocean circulation in a warming climate. *Nature*, *451*(7176), 286–288. <https://doi.org/10.1038/nature06590>
- Wakatsuchi, M., Ohshima, K. I., Hishida, M., & Naganobu, M. (1994). Observations of a street of cyclonic eddies in the Indian Ocean sector of the Antarctic Divergence. *Journal of Geophysical Research*, *99*(C10), 20,417–20,426. <https://doi.org/10.1029/94JC01478>
- Warnock, J. P., & Scherer, R. P. (2014). A revised method for determining the absolute abundance of diatoms. *Journal of Paleolimnology*, *53*(1), 157–163. <https://doi.org/10.1007/s10933-014-9808-0>
- Warnock, J. P., Scherer, R. P., & Konfirst, M. A. (2015). A record of Pleistocene diatom preservation from the Amundsen Sea, West Antarctica with possible implications on silica leakage. *Marine Micropaleontology*, *117*, 40–46. <https://doi.org/10.1016/j.marmicro.2015.04.001>
- Weber, M. E., Clark, P. U., Kuhn, G., Timmermann, A., Spreng, D., Gladstone, R., et al. (2014). Millennial-scale variability in Antarctic ice-sheet discharge during the last deglaciation. *Nature*, *510*(7503), 134–138. <https://doi.org/10.1038/nature13397>

- Weltje, G. J., & Tjallingii, R. (2008). Calibration of XRF core scanners for quantitative geochemical logging of sediment cores: Theory and application. *Earth and Planetary Science Letters*, *274*(3–4), 423–438. <https://doi.org/10.1016/j.epsl.2008.07.054>
- Williams, G. D., Meijers, A. J. S., Poole, A., Mathiot, P., Tamura, T., & Klocker, A. (2011). Late winter oceanography off the Sabrina and BANZARE coast (117–128 degrees E), East Antarctica. *Deep-Sea Research Part II-Topical Studies in Oceanography*, *58*(9–10), 1194–1210. <https://doi.org/10.1016/j.dsr2.2010.10.035>
- Wilson, D. J., Bertram, R. A., Needham, E. F., van de Flierdt, T., Welsh, K. J., McKay, R. M., et al. (2018). Ice loss from the East Antarctic Ice Sheet during late Pleistocene interglacials. *Nature*, *561*(7723), 383–386. <https://doi.org/10.1038/s41586-018-0501-8>
- Wilson, D. J., Struve, T., van de Flierdt, T., Chen, T., Li, T., Burke, A., & Robinson, L. F. (2020). Sea-ice control on deglacial lower cell circulation changes recorded by Drake Passage deep-sea corals. *Earth and Planetary Science Letters*, *544*, 116405. <https://doi.org/10.1016/j.epsl.2020.116405>
- Wright, A. P., Young, D. A., Roberts, J. L., Schroeder, D. M., Bamber, J. L., Dowdeswell, J. A., et al. (2012). Evidence of a hydrological connection between the ice divide and ice sheet margin in the Aurora Subglacial Basin, East Antarctica. *Journal of Geophysical Research*, *117*, F01033. <https://doi.org/10.1029/2011JF002066>
- Yin, Q., & Berger, A. (2015). Interglacial analogues of the Holocene and its natural near future. *Quaternary Science Reviews*, *120*, 28–46. <https://doi.org/10.1016/j.quascirev.2015.04.008>
- Young, D. A., Wright, A. P., Roberts, J. L., Warner, R. C., Young, N. W., Greenbaum, J. S., et al. (2011). A dynamic early East Antarctic Ice Sheet suggested by ice-covered fjord landscapes. *Nature*, *474*(7349), 72–75. <https://doi.org/10.1038/nature10114>
- Zielinski, U., & Gersonde, R. (2002). Plio–Pleistocene diatom biostratigraphy from ODP leg 177, Atlantic sector of the Southern Ocean. *Marine Micropaleontology*, *45*(3–4), 225–268. [https://doi.org/10.1016/S0377-8398\(02\)00031-2](https://doi.org/10.1016/S0377-8398(02)00031-2)